REPORT DOCUMENTATION PAGE

Form Approved OMB NO. 0704-0188

1. REPORT DATE (DD-MM-YYYY)	2. REPORT TYPE	3. DATES COVERED (From - To)
21-07-2014	MS Thesis	-

4. TITLE AND SUBTITLE
Photocurrent Cancellation due to Barrier Asymmetry in GaAs/AlGaAs heterostructure Infrared Detectors

5a. CONTRACT NUMBER
W911NF-12-2-0035

5b. GRANT NUMBER

5c. PROGRAM ELEMENT NUMBER
611102

6. AUTHORS
Justin Ryan Mclaughlin

5d. PROJECT NUMBER

5e. TASK NUMBER

5f. WORK UNIT NUMBER

7. PERFORMING ORGANIZATION NAMES AND ADDRESSES
Georgia State University
PO Box 3999

Atlanta, GA 30302 -3999

8. PERFORMING ORGANIZATION REPORT NUMBER

9. SPONSORING/MONITORING AGENCY NAME(S) AND ADDRESS (ES)
U.S. Army Research Office
P.O. Box 12211
Research Triangle Park, NC 27709-2211

10. SPONSOR/MONITOR'S ACRONYM(S)
ARO

11. SPONSOR/MONITOR'S REPORT NUMBER(S)
61772-EL.13

12. DISTRIBUTION AVAILIBILITY STATEMENT
Approved for public release; distribution is unlimited.

13. SUPPLEMENTARY NOTES
The views, opinions and/or findings contained in this report are those of the author(s) and should not contrued as an official Department of the Army position, policy or decision, unless so designated by other documentation.

14. ABSTRACT
Bi-directional photocurrent cancellation in a 30 period GaAs/AlxGa1-xAs split-off band photodetectors will be discussed. This cancellation results in a distinctive zero response "notch" in spectral responsivity curves that can be controlled over the entire response range of the detector by using applied bias voltage. This phenomenon occurs at low negative bias, indicating a built-in potential offset in the AlxGa1-xAs barriers, with higher potential occurring at GaAs-on-AlGaAs interfaces. This asymmetry is also shown in threshold wavelength difference between negative and positive applied bias, and shows increasing potential offset with increasing aluminum fraction of the AlxGa1

15. SUBJECT TERMS
Infrared, Photodetectors, Heterojunction, Splitoff, GaAs, AlGaAs, photocurrent cancellation, bi directional

16. SECURITY CLASSIFICATION OF:			17. LIMITATION OF ABSTRACT	15. NUMBER OF PAGES	19a. NAME OF RESPONSIBLE PERSON
a. REPORT	b. ABSTRACT	c. THIS PAGE			Unil Perera
UU	UU	UU	UU		19b. TELEPHONE NUMBER 404-413-6037

Report Title

Photocurrent Cancellation due to Barrier Asymmetry in GaAs/AlGaAs heterostructure Infrared Detectors

ABSTRACT

Bi-directional photocurrent cancellation in a 30 period GaAs/AlxGa1-xAs split-off band photodetectors will be discussed. This cancellation results in a distinctive zero response "notch" in spectral responsivity curves that can be controlled over the entire response range of the detector by using applied bias voltage. This phenomenon occurs at low negative bias, indicating a built-in potential offset in the AlxGa1-xAs barriers, with higher potential occurring at GaAs-on-AlGaAs interfaces. This asymmetry is also shown in threshold wavelength difference between negative and positive applied bias, and shows increasing potential offset with increasing aluminum fraction of the AlxGa1-xAs barriers.This barrier asymmetry is a major contributor to photovoltaic operation in otherwise symmetric device structures, and a thorough understanding of this phenomenon could lead to better operating and design parameters used for multi-junction photodetectors. It is also believed that bias-tuned multi-band detectors could be developed by taking advantage of this photocurrent directionality.

A STUDY OF PHOTOCURRENT CANCELLATION MECHANISMS IN GaAs / $Al_xGa_{1-x}As$ HETEROSTRUCTURE INFRARED PHOTODETECTORS

by

JUSTIN MCLAUGHLIN

Under the Direction of Dr. Unil Perera

ABSTRACT

Bi-directional photocurrent cancellation in 30 period GaAs/$Al_xGa_{1-x}As$ split-off band photodetectors will be discussed. This cancellation results in a distinctive zero-response “notch” in spectral responsivity curves that can be controlled over the entire response range of the detector by using applied bias voltage. This phenomenon occurs at low negative bias, indicating a built-in potential offset in the $Al_xGa_{1-x}As$ barriers, with higher potential occurring at GaAs-on-AlGaAs interfaces. This asymmetry is also shown in threshold wavelength difference between negative and positive applied bias, and shows increasing potential offset with increasing aluminum fraction of the $Al_xGa_{1-x}As$ barriers. This barrier asymmetry is a major contributor to the photovoltaic operation in otherwise symmetric device structures, and a thorough understanding of this characteristic could lead to better operating and design parameters used for multi-junction photodetectors.

A STUDY OF PHOTOCURRENT CANCELLATION MECHANISMS IN GaAs / $Al_xGa_{1-x}As$ HETEROSTRUCTURE INFRARED PHOTODETECTORS

by

JUSTIN MCLAUGHLIN

A Thesis Submitted in Partial Fulfillment of the Requirements for the Degree of

Master of Science

in the College of Arts and Sciences

Georgia State University

2014

A STUDY OF PHOTOCURRENT CANCELLATION MECHANISMS IN GaAs / $Al_xGa_{1-x}As$ HETEROSTRUCTURE INFRARED PHOTODETECTORS

by

JUSTIN MCLAUGHLIN

Committee Chair: Unil Perera

Committee: Vadym Apalkov

Joshua Von Korff

Alexander Kozhanov

Electronic Version Approved:

Office of Graduate Studies

College of Arts and Sciences

Georgia State University

May 2014

To my parents.

ACKNOWLEDGEMENTS:

The thesis work was supported in part by the US Army grant No. W911NF-12-2-0035 monitored by Dr. William W. Clark, and US National Science Foundation under grant No. ECCS 1232184 monitored by Dr. John Zavada.

TABLE OF CONTENTS

LIST OF TABLES

LIST OF FIGURES

1 INTRODUCTION

Any object that is above absolute zero (0 K) gives off thermal radiation, much of it in a region of the electromagnetic spectrum that is beyond the capabilities of our eyes to detect; the infrared region. A diagram of the electromagnetic spectrum is shown in Figure 1.1. There are many uses for infrared detectors, such as thermal imaging, fiber optic communications, weather satellite imaging, spectroscopy, astronomy, and thermal tracking.[1] For many of these applications, it is beneficial to have a robust, portable, and efficient detector as a basis for infrared detection.

In order to detect such radiation, a detector must be designed in a way which can absorb incoming light and turn it into an observable electrical signal. Detectors based on semiconductor materials have shown progress in being able to meet the goals of small size, efficiency, and uncooled operation. There are many different designs and materials for semiconductor photodetectors, and this study will focus on Split-off Band Infrared Detectors. In particular, it will analyze an anomaly found in the spectral response of these detectors at low bias operation.

1.1 Experimental Reasoning

While testing the spectral response of one of our detectors, an anomaly was observed, shown in Figure 1.2. It soon became evident this anomaly was dependent on the applied bias of the detector, temperature, and the external circuit load resistance and hence a property of the device. Due to spectral responsivity behavior, it was hypothesized that this anomaly was the result of photocurrent cancellation in the detector. Further investigation showed that this was observed in other detectors that our group had designed. It was not entirely understood why this anomaly should occur, so its origins were investigated.

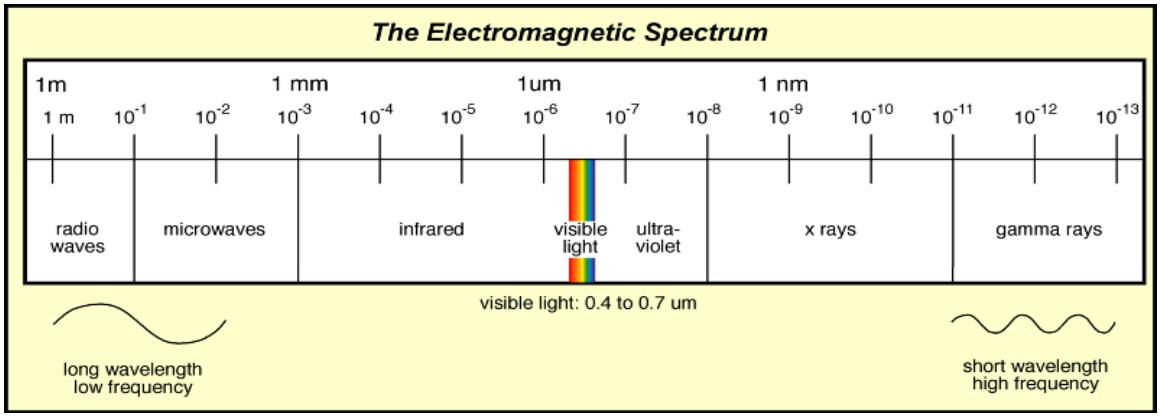

Figure 1.0.1: The Electromagnetic Spectrum. Frequency and energy increase moving toward the right side of the diagram, while wavelength becomes shorter. The infrared band of the spectrum can be seen immediately to the left of visible light. (*Image courtesy of Columbia University, http://www.columbia.edu/~vjd1/electromag_spectrum.htm*)

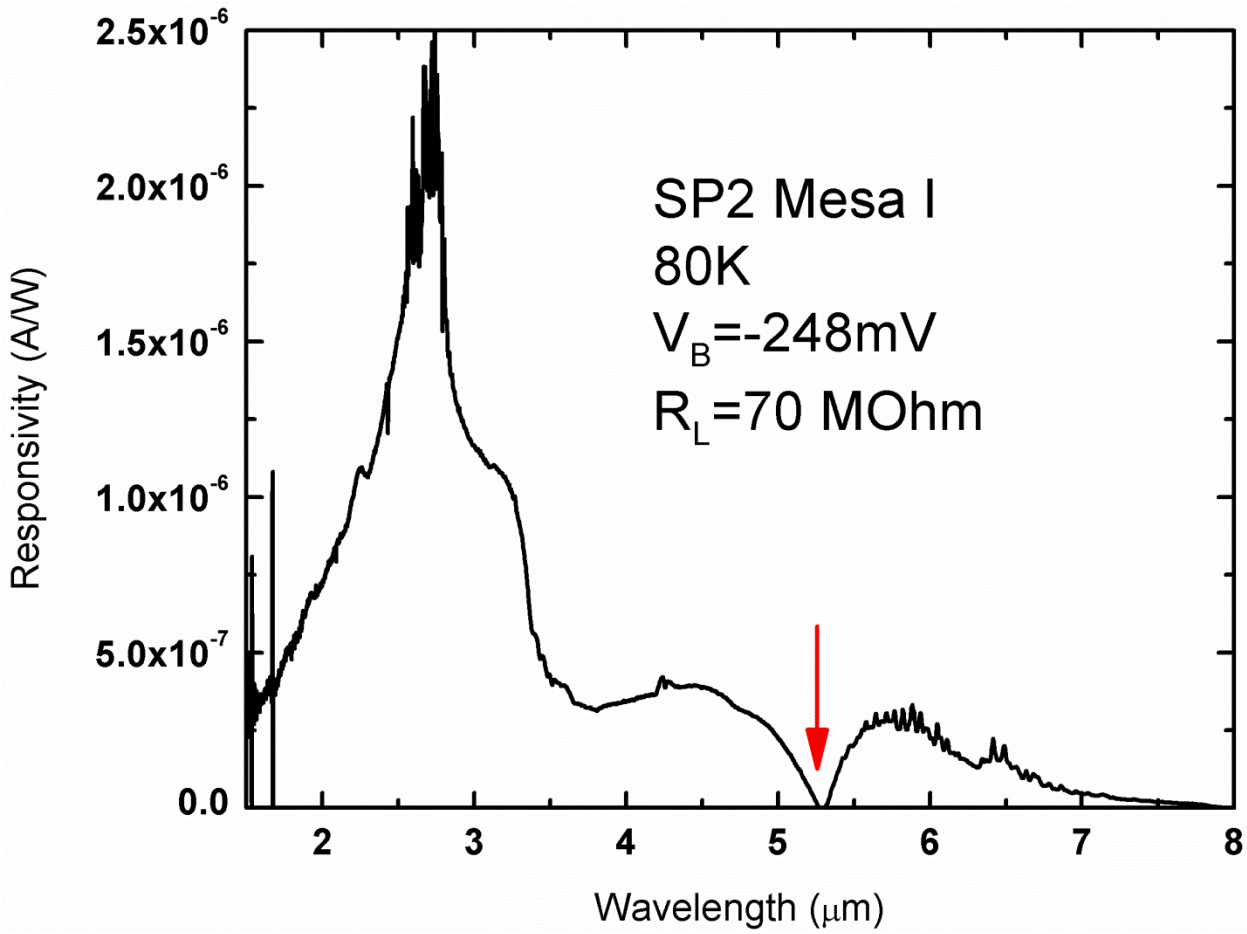

Figure 1.0.2: Responsivity of SP2 Mesa I showing the notch in the spectrum. The purpose of this study is to determine the cause of this anomaly. Detector temperature is 80K, bias voltage is -248 mV, and a 70MΩ load resistor is used.

1.2 Experimental Goals

This thesis attempts to meet the following goals:

- To understand the origin of this anomaly, by analysis of the optoelectronic properties of the detectors being studied.
- To model the optoelectronic properties of the device to attempt to recreate such an anomaly via theory.
- To address concurrent issues that have manifested- such as the dependence of notch position on load resistance.

2 BACKGROUND

Infrared radiation, or light, was first discovered in 1800 by the German born scientist, Sir Frederick William Herschel while he was trying to find a relationship between thermal energy and the color of visible light.[2] Using a prism to break sunlight into its constituent colors, he placed a thermometer under each of the projected colors to record the temperature. Another thermometer was placed outside of the projected light to act as a control for the experiment, by measuring the ambient temperature of the room. Surprisingly, this reading showed a higher temperature than the visible light being tested. After further experiments to test the properties of this "invisible light," Herschel concluded that there was light beyond the red part of the visible spectrum. This light beyond red was called Infrared.

Infrared was the first electromagnetic radiation detected by humans outside of the visible range of the eye. As it would turn out, the universe and the world around us was constantly producing this radiation in various wavelengths, yet had gone undiscovered. In fact, the light that we can actually *see* with our eyes is but a small portion of the entire electromagnetic spectrum, as shown in Figure 1.1. Electromagnetic radiation with higher energy than that of visible light consists of ultraviolet, x-rays, and gamma rays, while radiation of lower energy than visible light consists of infrared, microwave, and radio waves. The infrared spectrum is of importance because it contains what is often to be considered "heat". Molecules absorb and emit electromagnetic waves in this region, and as such, can be "seen" if an eye can be created to specifically detect these signals.

2.1 Detection of Light

In order to detect electromagnetic radiation that is outside the visible range, a detector must be designed which is sensitive to the light in question. Light can be characterized by three

different quantities, each of which is directly related to the other, and any one can be used. When light is referred to as a wave, it can be described by either its wavelength, or frequency, which is inversely proportional to wavelength. When discussing light in the quantum framework, one refers to the energy it carries (photon or quanta.) The relation between these three is given as:

$$E = h\nu = \frac{hc}{\lambda} \tag{1.1}$$

where E is the photon's energy , h is Planck's constant, ν is the wave's frequency, and λ is it's wavelength.

It had been known since the late 19th century that light can interact with metal. In particular, certain metals, when exposed to highly energetic light, such as ultraviolet, will produce electricity. This occurs via a process called the Photoelectric effect, which was explained by Albert Einstein in 1905, for which he later earned the Nobel Prize in Physics.[3] If a photon, the particle that makes up light, impacts a particular metal with enough energy, it can release an electron from its bond, producing electricity.

This knowledge was used to make vacuum tubes that could effectively detect light, and convert it into an electronic signal. However, vacuum tubes are relatively large, fragile, and require high voltages to operate. With the dawn of semiconductor technology, vacuum tubes of all types began to be replaced in electronics by semiconductor devices, which were more robust mechanically, smaller, required less voltage, and as the technology improved, cheaper to make.

2.2 Semiconductor Detectors

In electrical conductivity, there are two categories of materials- conductors and insulators. Materials such as rubber, and wood, could not conduct electricity, whereas metals easily pass, electricity through them. But another type of materials was discovered that was not fully in either of these previous categories-- materials that showed increasing conductance with tempera-

ture, opposite to metals, and would share characteristics between the conductors and insulators.[4] These materials became known as semiconductors.

By making semiconductor "switches" or transistors, smaller and smaller, computers were able to increase speed and complexity, all the while decreasing in size and electricity consumption. The transistor has often times been described as the most important invention of the 20th century, as it single-handedly ushered in the Information Age.

When atoms are arranged in a material, the nucleus of an atom is surrounded by electrons, which form bonds between the other atoms in the material. If the electrons are given high enough energy, by absorbing a photon, they can "break away" from the atom and move freely within the material. When the electrons move freely, this is called conduction. The valence band is the energy level that the electrons occupy when bound to their atoms, where the conduction band are the energy levels where electrons are free to move, and conduct. In a conductor, the valence band and conduction bands overlap, meaning that little to no energy is required to have electrons break away and they are free to move through the material. In an insulator, however, there is a large energy gap between the valence and conduction bands- electrons require more energy to get into the conduction band, therefore electrons do not easily travel through the material. A semiconductor does have a separation between these two bands, but the energy gap is much lower than that of an insulator. So for a semiconductor to conduct electricity, there just needs to be enough energy to be able to excite the electron into the conduction band.

At its most basic, a semiconductor photodetector works via the following process: (*i*) a photon with energy at, or higher than, the energy gap of the semiconductor incident on the material and is absorbed by an electron in the valence band (*ii*) energized, the electron is now in the conduction band, and (*iii*) a voltage is applied across the semiconductor which creates an electric

field, which sweeping the electron in the direction opposite of the field. This type of device is commonly referred to as a photoconductor. In the absence of light, conductivity is greatly reduced, so the material acts more like a resistor, however, when light is present, electrons are energized and free to flow through the material, so the device now behaves like a conductor.

While this type of detector benefits from simplicity, it is dependent on the material's energy gap, which restricts the range of usefulness depending on application, as there is a limited number of materials that can be used. Depending on the specific application, often times more complex devices have to be created to meet the goals for photodetection.

2.3 Semiconductor Materials

Many different types of materials can display semiconductor properties, and in designing a detector, the material selection is often the first consideration- in conjunction with the particular detection mechanism. The most common semiconductors are pure elements, and various compounds of elements from different groups of the periodic table. The single –element, or pure element semiconductors are from Group IV of the periodic table, with silicon and germanium being quite common. The binary compound semiconductors are often referred to by the groups of the periodic table they are comprised of, such as III-V (a compound of an element from Group III and an element from Group V) compounds.

These materials will have a characteristic band gap energy, which can be useful in the selection process for particular applications. Furthermore, there are other characteristics that may make a material more or less appropriate for a detector. Gallium Arsenide (GaAs), a III-V compound widely used for various applications, has a much greater electron mobility than Silicon, which gives it a faster response time. The III-V compounds of gallium arsenide and aluminum

gallium arsenide (AlGaAs) are the principle materials used in this study of detectors. Here the focus will be their particular characteristics and usefulness.

2.3.1 Crystal Lattice

A common characteristic of inorganic elemental semiconductors is their crystalline structure. When the material is formed, the atoms naturally arrange themselves in an ordered structure, which produces a repeating pattern of atomic placement throughout the material. The crystalline structure of GaAs is of the type zincblende, as seen in Figure 2.1.

The dimension of the unit cell, *a* in Figure 4, is the spacing between repeating structures of the crystal formation, called the lattice constant. This parameter is important when joining different compounds together- the lattice constant should match as much as possible between two materials, so as to not introduce strain in the material and produce negative electrical effects. A graph showing the major compound semiconductors, and the relation between the bandgap energy and lattice constant can be seen in Figure 2.2.

Another important characteristic of semiconductors is the ability to add impurities to the material to affect electrical and optical properties. A pure material is referred to as an intrinsic, whereas when impurities are added, it is called extrinsic. These impurities, called dopants, are intentionally added to the otherwise pure material through a process called doping. The impurities are selected in order to increase charge carriers in the material, either electrons or holes. A hole is the absence of an electron- which behaves as a positively charged analogue to the electron. GaAs is often doped with Silicon in order to increase electron concentration, or Beryllium to increase hole concentration. An extrinsic semiconductor with increased electron carriers is referred to as n-type, whereas increased hole carriers is called p-type.

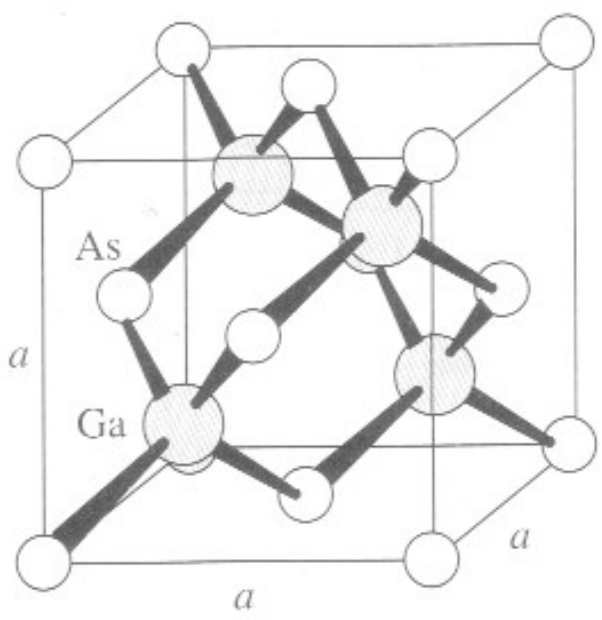

Figure 2.1: A GaAs unit cell. This is the repeating structure found in a crystalline formation of Gallium Arsenide. The lattice constant is denoted as a.

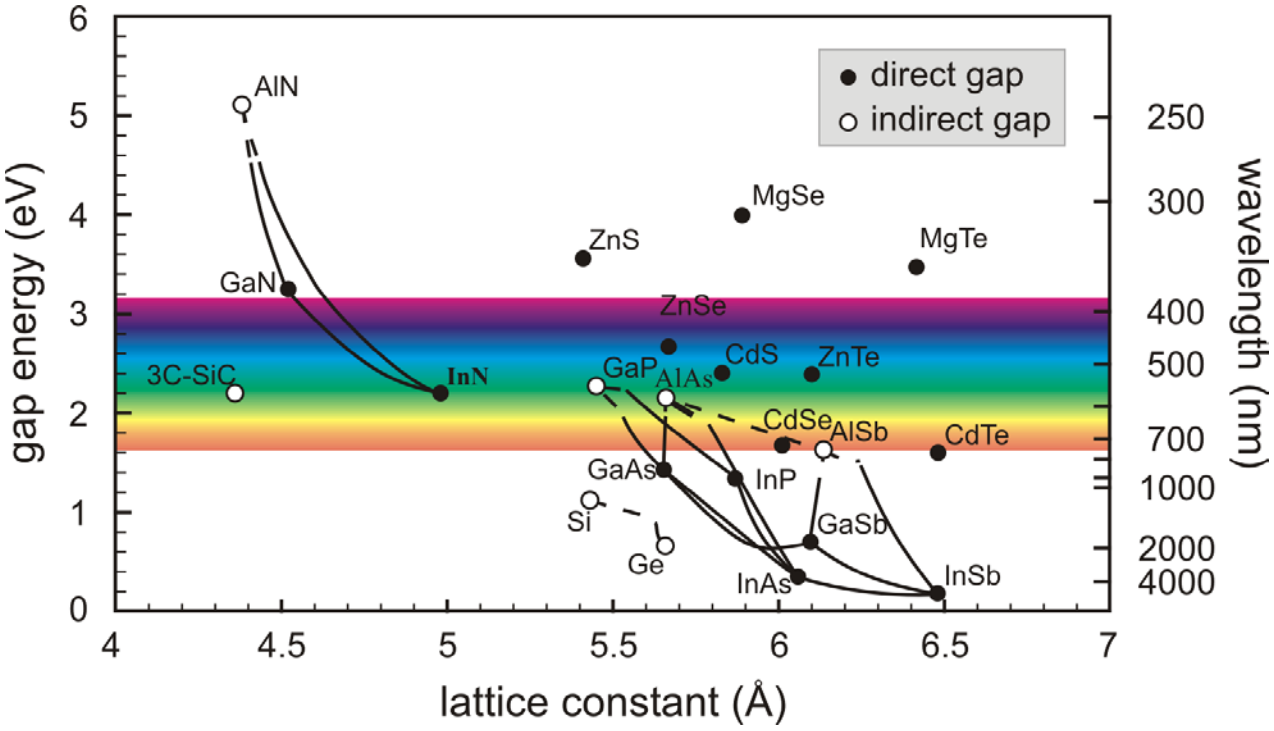

Figure 2.2: Compound semiconductors and relation between band gap energy and lattice constant.

2.4 Semiconductor Growth

The manufacture of semiconductor devices is a complex and highly specialized engineering discipline. The creation of such devices is often referred to as semiconductor "growth," as the material is often made layer by layer, and always under special conditions in order to form the crystalline lattice and multi-layered structure needed. Due to the small scale of most semiconductor devices, and critical reliance on pure materials in order to match expected design conditions, various techniques have been developed in order to manufacture semiconductor devices, each with their own advantages and disadvantages. It is important to have some understanding of these processes so that suggestions can be made before fabrication, as well as an understanding of the device during the testing phase, as different processes can yield different results.

In order to grow a multi-layered detector, one must first start with a proper foundation. This base layer is called a substrate, or wafer. The substrate is used for structural support of the end device, as the active layers of the device are incredibly small, as well as providing a lattice structure to properly align the layers that will ultimately be grown on top of the wafer. Wafers are grown via the Czochralski process, in which a highly pure semiconductor, in most cases silicon, is melted in a crucible.[5] A rod with an attached "seed crystal" is inserted into the molten silicon, then slowly turned and pulled out. The end result is a cylindrical ingot of pure, crystalline silicon. The ingot is then sliced to produce the circular wafers, then finally polished. Often the wafers are sold commercially to other semiconductor growers so that the next step can proceed.

2.4.1 Epitaxy

In order to grow thin, multiple layers of varying materials, a different process is required than used in the growth of a single crystalline wafer/substrate. This is called epitaxy,

from the Greek “to arrange upon,” which involves depositing a thin layer of a semiconductor on top of the substrate.[6] The new layers will align along the direction in the substrate, which is determined ahead of time. There are multiple techniques of epitaxial growth, based on the method of layer deposition, two of which will be described.

Metalorganic chemical vapor deposition (MOCVD) is a deposition method that relies on chemical reactions to create crystalline layers of semiconductors on top of a substrate. Sometimes it is also referred to as metalorganic vapor phase epitaxy (MOVPE) or organometalic vapor phase epitaxy (MOVPE).[7] The growth process involves the flow of gaseous precursors over a substrate, which undergo chemical reactions in order to deposit layers of the desired semiconductor on top of the substrate. The process takes place in a reactor, where the gases are incorporated to flow over the substrate. The main advantage of MOCVD is the fast growth rate (2-100 μm/hour) of the films.[8] Also, the reactions take place near atmospheric pressure, so a high vacuum is not needed- the purity of the precursor gases is important for reducing impurities. However, some disadvantages are also present. The precursors for many materials are extremely toxic gases. This means special safety and environmental disposal considerations must be taken. Also, the ability to monitor the growth process is not as precise as other methods. This is fine when growing bulk semiconductors quickly, where depth is not critical, but not optimum when trying to grow exact depths (monolayers of thickness).

Molecular beam epitaxy (MBE) is another commonly used epitaxial growth technique, or direct method of deposition. It requires that the substrate be placed in an ultra-high vacuum chamber to keep impurities low. Because of this low pressure, the substrate can also be heated to a lower temperature (~550 degrees Celsius) than in MOCVD.[9] Around the chamber are smaller chambers where pure, solid elements for deposition are heated. Once heated, the molecules begin

to sublimate into a gas. Because of the low pressure, the mean free path of the molecules is very long (meters) and form a "beam" of molecules converging onto the substrate.[6] A mechanical shutter controls the molecular beam. While MBE is not as versatile as MOCVD, requires a very high quality vacuum, and has higher equipment costs, there are some advantages. Because of the UHV, extremely high purity can be achieved during growth. Also, while the growth process is slow for MBE (~1 monolayer /second), the deposition can be precisely controlled allowing for abrupt changes in the deposited layers. This means that abrupt junctions can be grown in layered structures. Also, in situ measurements can be done on the wafer, allowing for measurement of the growth rate and depth.[10] The devices that will be detailed in this study were grown via MBE. As it turns out, it the method employed during device growth does have an impact on the physics of the finished product, as we will see later. This is particularly true at the interface, or junction, between two materials in a multi-layered structure.

2.5 Infrared Photodetectors

The visible spectrum ends at a wavelength of 700 nm, or an energy of 1.7 eV, where the infrared spectrum begins. In order to detect photons in this range, the detection mechanism must take place at energies less than 1.7 eV. However, this is lower than many bandgap energies of the intrinsic semiconductors, so other modes of absorption are required in the long-wavelength, low-energy regime. Some methods are based on material properties, such as impurity level transitions, intraband transitions, and free-carrier absorption (FCA.) Another way is through engineering structures that take advantage of quantum confinement to create sub-band and mini-band transitions, as demonstrated in quantum well infrared photodetectors (QWIPs,) multiple quantum well (MQW,) and superlattice structures.

2.5.1 Heterojunction Interfacial Workfunction Internal Photoemission Detectors

Heterojunction interfacial workfunction internal photoemission (HEIWIP) detectors consist primarily of a highly p-doped GaAs emitter next to an $Al_xGa_{1-x}As$ barrier, which forms a workfunction at the junction due to the valence band offset (VBO) between the two materials. The interfacial workfunction is governed by the aluminum fraction in the barrier and determines the cut-off wavelength (λ_c) of the detector. The method of detection for HEIWIPs is: (i) absorption of light via free-carrier absorption, and (ii) provided there is sufficient energy to overcome the workfunction, subsequent emission over the barrier and collection.[4]

The device structures are 16 periods of 188 Å GaAs emitter and 1250 Å $Al_xGa_{1-x}As$ barrier heterojunctions, between a 0.2 μm GaAs top contact and a 0.7 μm GaAs bottom contact. The contacts were Be doped to 1 X 10^{19} cm^{-3}. The devices were grown via molecular beam epitaxy (MBE) and the barriers have an aluminum fraction of x=0.12. The three detectors, named HE0204, HE0205, and HE0206, had varied emitter doping levels, of 10, 3, and 1 X 10^{17} cm^{-3}, respectively.[5]

While superlattice and multiple quantum well detectors utilize periodic structures to exploit quantum confinement to create sub-bands and minibands for detection, HEIWIPs use multiple periods to increase response. To increase responsivity in a detector, one could increase the number of carriers available for detection. This can be accomplished by either increasing the doping level of an extrinsic semiconductor, or by increasing the amount of material in the active layer in the device, which also increases carriers available. However, there is a limit to the how much a semiconductor can be doped, and increasing the depth of an emitter level cannot be done arbitrarily, as scattering will become an issue and negate the usefulness of an increased emitter length. The scattering length indicates the probability that carrier will be scattered during travel,

in turn losing energy, and is dependent on the material through which the carrier is traveling. The shorter the scattering length of a material, the shorter the useful emitter length can be because if the emitter is much larger, carriers which are given enough energy to overcome the barrier at the opposite end of the emitter may end up losing the required energy by the time it reaches the barrier. So to overcome this, multiple periods of emitter/barrier heterojunctions can be used to effectively increase the active layer of the device.

The HEIWIP free carrier detectors were not a part of this particular study. However, they were the precursors to the detectors that were used. While HEIWIPs utilized free-carrier absorption, and were designed for long-wavelength infrared detection, shorter wavelength transitions were observed as well. It was determined that these shorter wavelength features were due to intraband transitions, and new detectors were designed to take advantage of this.

2.5.2 Split-off Band Detectors

Split-off band detectors share similar device architecture to HEIWIPs, yet differ in some respects due to the difference in the mode of absorption. The split-off band detectors take advantage of intervalence band (IVB) transitions which occur in the 2-10 μm range for the p-doped GaAs emitters, which are more highly doped at 3 X 10^{18} cm^{-3}. Since the detection range occurs at higher energy, the barriers can be increased via higher aluminum fraction, which also provides better suppression of thermal dark current. In fact, one of the detectors is able to operate at T=300K, allowing for uncooled operation.

The detectors under study consist of 30 periods, p-type (N_A=3×10^{18}) GaAs/$Al_xGa_{1-x}As$ heterojunctions. All three detectors share the same device architecture as seen in Figure 3, but vary in aluminum fractions in the $Al_xGa_{1-x}As$ barriers, with parameters listed in Table I. The three samples are labeled SP1, SP2 and SP3 and have aluminum fractions of x = 0.28, 0.37, and 0.57,

giving threshold wavelengths of 9.3 µm, 6.5 µm, and 4.1 µm respectively.[6] Device architecture is shown in Figure 2.3.

Table 2.1. Device Parameters of the split-off band photodetectors under study. Potential offset, Δp, was measured by comparison of threshold wavelength between positive and negative bias conditions, and is discussed in the Results section.

Sample No.	Al fraction (x)	λ_t (μm)	Load Resistance (MOhm)	Bias Range (negative mV)
SP1	0.28	9.3±0.3	6	150-210
SP2	0.37	6.5±0.3	2	225-500
			6	~200-400
			10	120-300
			70	50-110
SP3	0.57	4.1±0.2	2	155-300
			10	60-180
			70	0–50

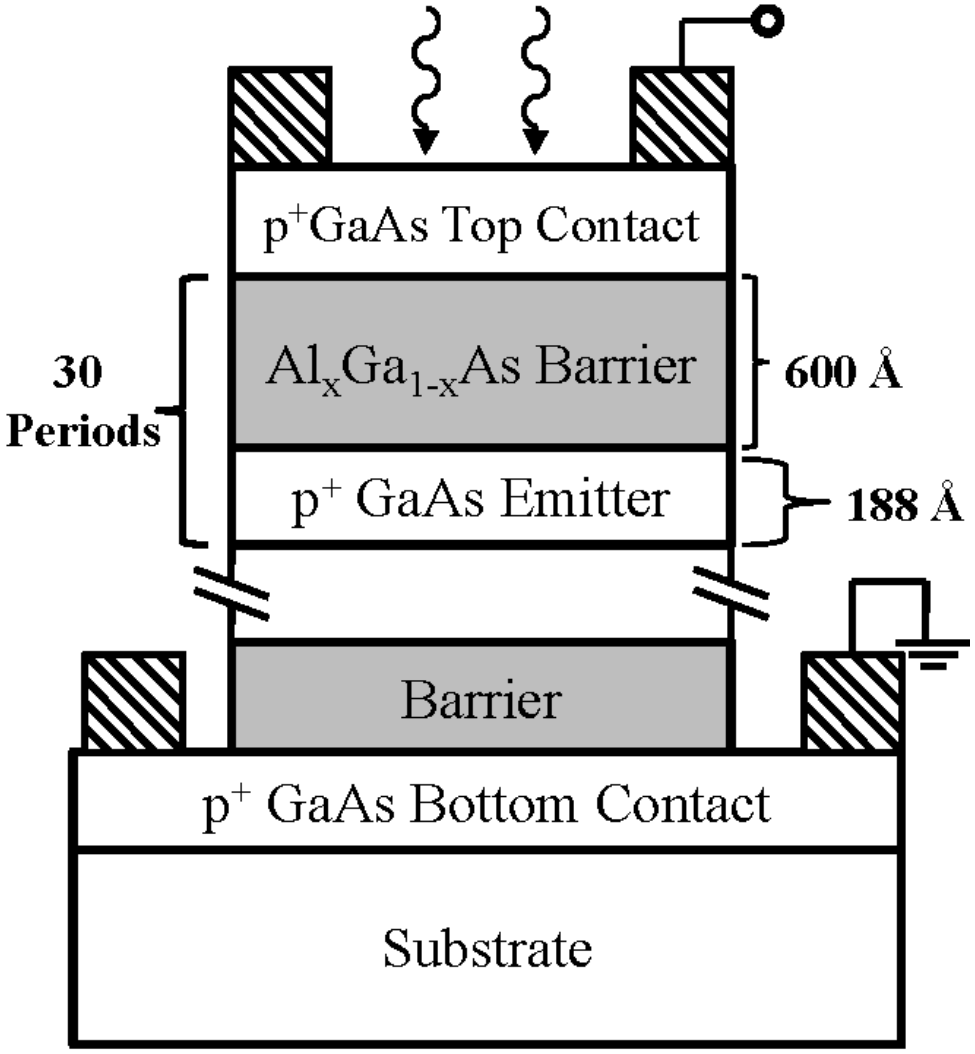

Figure 2.3 Device architecture of the reported detectors. All three detectors comprise of highly-doped (NA=1×1019) p-type GaAs top and bottom contact layers. Between these layers are 30 periods of 188 Å p-type (NA=3×1018) GaAs emitters and 600 Å undoped AlxGa1-xAs barriers which form a heterojunction. The three detectors differ in aluminum fraction, x (= 0.28, 0.37, 0.57 for SP1, SP2, SP3, respectively), of the AlxGa1-xAs barriers.

3 RESULTS

The notch, shown earlier in Figure 1.2, is believed to be due to photocurrent cancellation between the two directions that flow in the detector. The qualitative reasoning for this is as follows:

During spectral response measurements and starting with zero applied bias, as positive bias is applied to the device (with respect to the top contact) the response increases. When negative bias is applied, however, initially the response decreases, with long wavelength response decreasing more than the short wavelength response. Negative bias device response for SP3 is shown in Figure 3.1. A notch in the spectral response then appears, and moves toward shorter wavelength as negative bias is increased. As negative bias is increased further, along with the notch movement, it is observed that response decreases for wavelengths shorter than the notch position, and increase for wavelengths longer than the notch position. Finally, once the notch has moved past the shortest wavelength of detector response, the entire response spectrum increases with increasing negative bias- much like it does for increasing positive bias.

Net photocurrent is the sum of the two major current contributions in the split-off detectors, forward- (current flow from top to bottom contact, i_{FOR}) and reverse- (current flow from bottom to top contact, i_{REV}) photocurrents. Detector responsivity is due to the net photocurrent that flows in the device under illumination. Forward (reverse) photocurrent becomes the dominant component of net photocurrent as high positive (negative) bias is applied, as shown in Figure 3.2. However at low bias, the two directional photocurrents are more evenly matched, which can result in zero net photocurrent if both forward and reverse currents are equal in magnitude. This cancellation is observed in detector response curves as a result of equal magnitudes between the two photocurrent directions for a particular wavelength in the device responsivity.

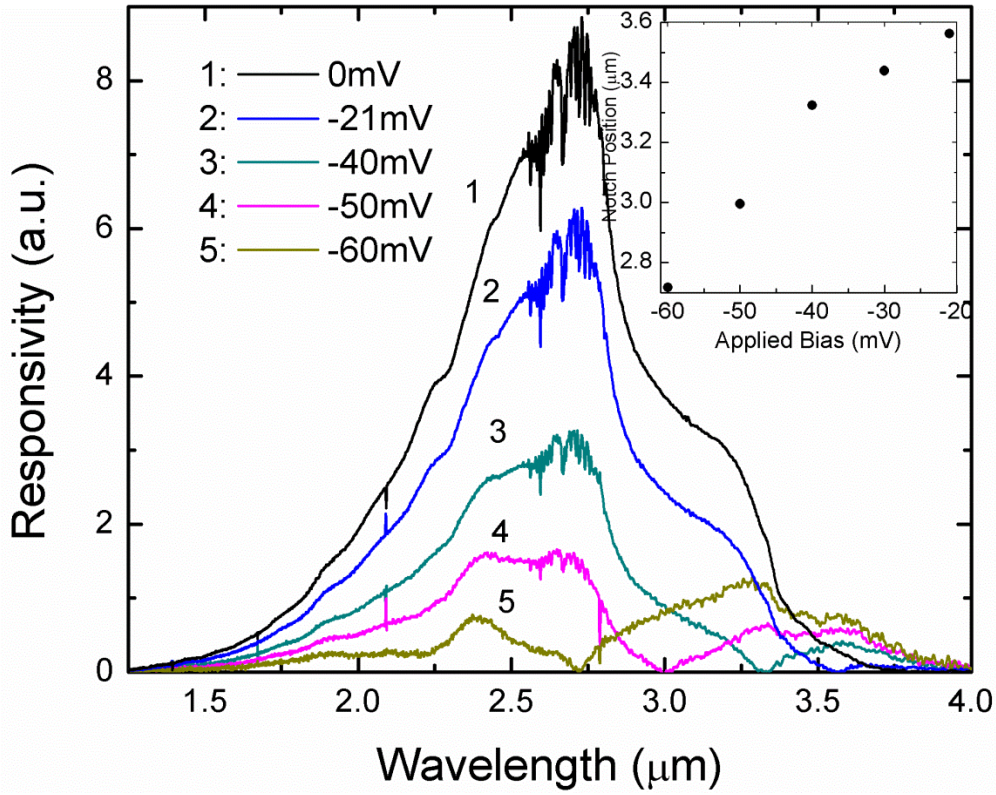

Figure 3.1: SP3 detector response at 80K for negative applied bias. Notch and response dynamics are shown for increasing negative bias, which decreases overall signal. With increasing bias, response for wavelengths shorter than the notch continues to decrease, while response at longer wavelengths begin to increase. The notch marks a separation between net forward photocurrent (wavelengths shorter than the notch) and net reverse photocurrent (wavelengths longer than the notch.) Inset shows the notch position, in μm, as a function of applied bias, in mV.

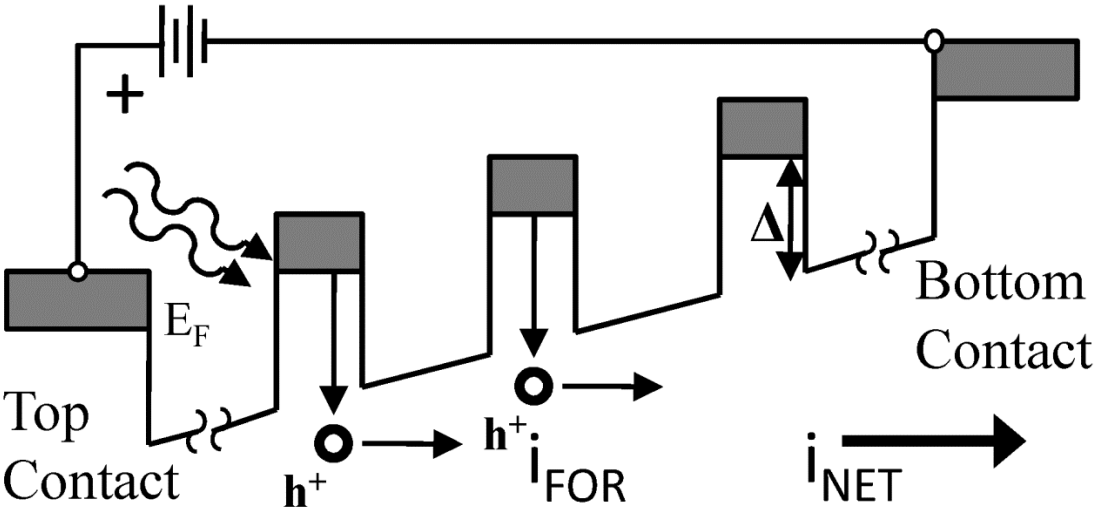

Figure 3.2: Band structure for split-off band detectors with positive applied bias. A bias is applied to the detector- polarity with respect to the top contact. For positive bias, excited carriers (holes in this case) are swept out via the electric field toward the bottom contact, which is considered forward photocurrent. For negative bias, carriers would be swept in the opposite direction, or reverse photocurrent.

When the notch is present in the spectrum, the device is undergoing a transition from forward photocurrent to reverse photocurrent. This is not immediately understood from responsivity measurements because the spectrum taken during Fourier Transform Infrared Spectroscopy (FT-IR) cannot resolve current polarity in the detector. Understanding of the notch dynamics, along with the net photocurrent directionality due to carrier sweep out under bias, polarity can be reconstructed from the response measurements to show a more intuitive picture of device response, shown in Figure 3.3.

It can be seen that forward photocurrent is still dominant into the negative bias operating range, indicating some type of offset as the transition does not occur at zero. In order to determine the cause of this, photoyield is calculated in *Mathematica*® by modeling photoemission.

3.1 Photoemission Modeling

To model the photocurrent cancellation, quantum efficiency (or photoyield) was calculated for forward and reverse current directions. Total quantum efficiency is found by calculating[7] three contributions, (i) internal quantum (or emission) efficiency, η_i, (ii) absorption efficiency, η_a, and (iii) collection efficiency, η_c, calculated separately for each direction of current flow. This results in the total quantum efficiency of the device:

$$\eta = \eta_a \eta_i \eta_c \tag{3.1}$$

In order to differentiate between the two current directions, a simplified model consisting of a single barrier separating two emitter/collectors was considered. Differences in effective workfunctions between the two directions were obtained by calculating the potential barrier, with the band profile shown in Figure 3.4. Previous work on Si p-i-n photodetectors provided the basis for this calculation.[7]

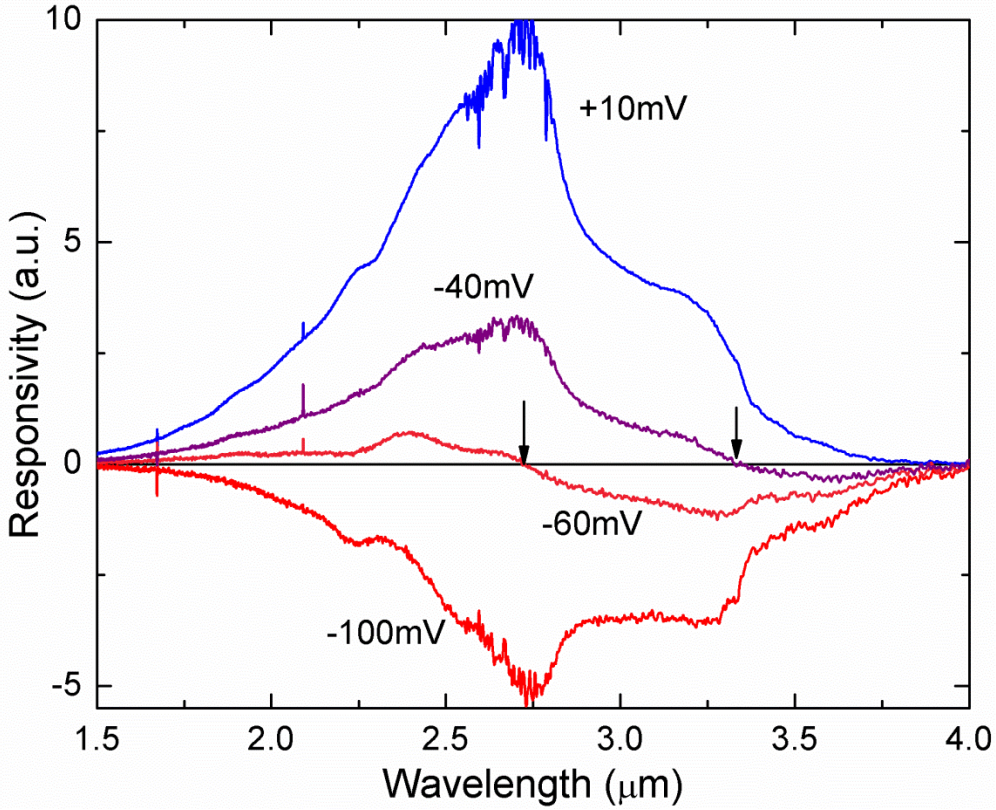

Figure 3.3: SP3 detector responsivity at different bias voltages with current polarity added manually. Positive responsivity represents current in the forward direction, while negative responsivity is reverse photocurrent. This shows better continuity between spectra for different biases. The notch position is marked by arrows. It is clear that forward photocurrent is "preferred" as fully switched direction does not occur until around -100 mV.

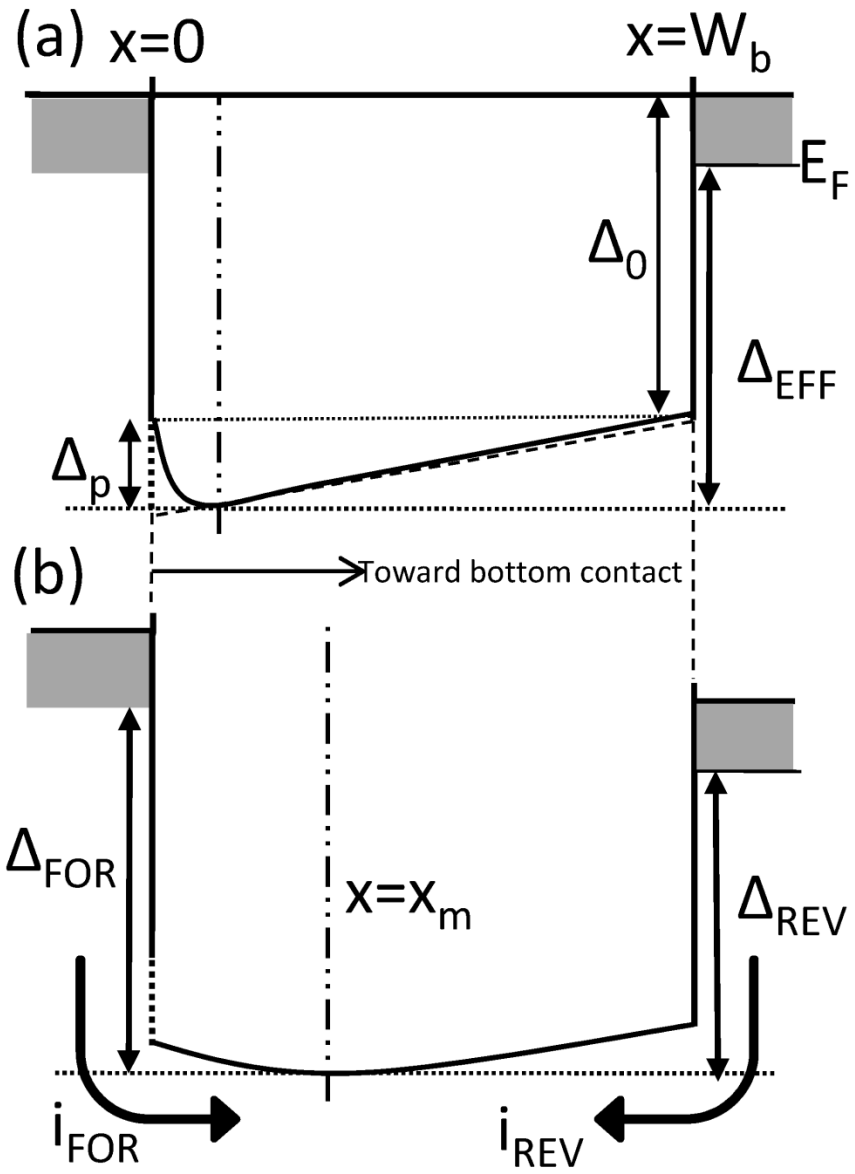

Figure 3.4: Potential barrier profile used in calculation (a) at zero applied bias. Δ_p is the barrier offset used in the calculation. Δ_{EFF} is the effective workfunction, which is equal on both sides at zero applied, but collection efficiency differs between the two sides due to the location of barrier maximum, x_m. Under low, negative bias (b) the condition for the notch to occur in the spectrum. Here the applied bias gives the reverse effective workfunction Δ_{REV} a lower energy than the forward effective workfunction Δ_{FOR}. This means the reverse direction has a higher emission efficiency. However, due to the barrier offset, the forward current direction, i_{FOR}, sees a shorter distance from interface to barrier maximum, resulting in higher collection efficiency than the reverse direction. This split in directional efficiency results in the spectral notch seen in response.

Unlike the p-i-n structures, the space-charge effect on the barrier profile is not present in the split-off detectors. The potential barrier has three contributions to its shape: valence band offset, applied electric field, and multiple image force lowering, with an additional contribution via a potential barrier offset added to one side of the barrier in order to account for the forward-direction preference seen in net photocurrent at zero bias.

The multiple image force potential lowering, as a function of position in the barrier can be approximated to first-order as[8]

$$\phi_i(x) = -\frac{q^2 W_b}{16\pi\epsilon_0\epsilon_s x(W_b - x)} \tag{3.2}$$

where W_b is the barrier width, q the electron charge, and x is the distance from the interface, which is shown in Figure 3.4. Including all contributions, the potential becomes

$$\phi(x) = \Delta_0 + q\bar{F}x + \phi_i(x) + \frac{\Delta_p}{W_b}(W_b - x) \tag{3.3}$$

where Δ_0 is the valence band offset between the emitter and the barrier, $\bar{F}$ is the electric field average due to applied bias, and Δ_p is the barrier/potential offset.

Internal quantum (emission) efficiency is the probability that a charge carrier is emitted over the interfacial barrier, which for HEIWIP or split-off detectors is typically described by the escape cone model[9, 10]. The model is based on the fraction of carriers that are first excited in the emitter then incident upon the barrier. If the carrier is of sufficient momentum, as determined by the component of momentum normal to the plane of incidence, the carrier will be successfully

emitted. In the event that a carrier does not successfully emit, it will be redirected via scattering events, losing energy in the process- but can be successfully emitted if it is redirected into the escape cone with the required momentum. Similar calculations were previously performed in initial modeling of the split-off detectors[11] and is covered thoroughly in the modeling of photoemission in THz detectors[12]. The ideal emission efficiency, η_{ideal}, and maximum efficiency, η_M, which is the ratio of hot carriers capable of being captured to the total number of photoexcited carriers is calculated via the escape cone model.

For systems where the effective workfunction, $\Delta > E_F$:

$$\eta_{ideal} = 0 \qquad (h\nu \leq 0)$$

$$\eta_{ideal} = \frac{3}{4}\frac{2}{3}\frac{[(E_F+h\nu)^{3/2}-(E_F+\Delta)^{3/2}]-(h\nu-\Delta)\cdot(E_F+\Delta)^{1/2}}{(E_F+h\nu)^{3/2}-(h\nu)^{3/2}}$$

$$\eta_M = \frac{1}{2}\cdot\frac{(E_F+h\nu)^{3/2}-(E_F+\Delta)^{3/2}}{(E_F+h\nu)^{3/2}-(h\nu)^{3/2}} \qquad (\Delta \leq h\nu < E_F+\Delta) \qquad (3.4)$$

$$\eta_{ideal} = \frac{3}{4}\frac{2}{3}\frac{[(E_F+h\nu)^{3/2}-(h\nu)^{3/2}]-E_F\cdot(E_F+\Delta)^{1/2}}{(E_F+h\nu)^{3/2}-(h\nu)^{3/2}}$$

$$\eta_M = \frac{1}{2} \qquad (E_F + \Delta \leq h\nu) \tag{3.5}$$

where $h\nu$ is the energy of the incident photon, E_F is the Fermi energy, and Δ is the effective workfunction.

The fraction of carriers that are successfully emitted before undergoing any scattering events in the emitter is given as:

$$\eta_0 = \frac{L^*}{W} \cdot \left(1 - e^{-\frac{W}{L^*}}\right)^{1/2} \cdot \eta_{ideal} \tag{3.6}$$

where L^* is the reduced scattering length for a hot carrier, and is a function of scattering lengths of cold electrons (L_e) and phonons and impurities (L_p) :

$$L^* = \frac{L_e L_p}{L_e + L_p} \tag{3.7}$$

For each scattering event, energy is lost and probability of emission reduced. To account for each subsequent scattering event, the total internal quantum efficiency becomes a series:

$$\eta_i = \eta_0 + \left[1 - \frac{\eta_0}{\eta_M}\right] \gamma \eta_1 + \left[1 - \frac{\eta_0}{\eta_M}\right] \cdot \left[1 - \frac{\eta_1}{\eta_M}\right] \gamma^2 \eta_2 + \cdots \tag{3.8}$$

where the amount of terms in the series is determined by the effect of "thermalization," $\eta_n = \eta_0(E - nh\nu)$, limits amount of scattering events a carrier can undergo before it loses enough en-

ergy to no longer be able to successfully undergo emission. The term $\gamma = \frac{L_e}{L_e+L_p}$ is the probability of a carrier scattering with a phonon before collision with a cold carrier.

Collection efficiency is the probability of a carrier successfully travelling from the emitter/barrier interface after emission to the barrier maximum without scattering. The distance from interface to barrier maximum, x_m, is calculated from Eq. 3 using the condition $\frac{\partial \phi}{\partial x} = 0$ for the given field present in the detector. By approximating the carrier's momentum to be normal to the interface (a selection criterion given by the first process in the escape cone model) the collection efficiency becomes

$$\eta_c = e^{-x_m/L_s} \tag{3.9}$$

where L_s is the scattering length in the barrier, which has been approximated as having no energy dependence. It is also assumed that there are no multiple reflections or scattering events. Absorption efficiency of the material was calculated previously[11], and is based

3.2 Discussion

The notch occurs at low, negative applied bias, typically $0 > V_b > -500$ mV, which suggests an offset in the barriers, as forward photocurrent is still dominant between zero bias and the point at which the notch occurs. It first appears at the long wavelength end of the device spectrum, and moves to the shorter wavelengths with increasing negative bias. Whenever the notch is present in the response curve, it indicates the switch from forward-current dominance (positive bias operation) to reverse-current dominance in net photocurrent (negative bias operation). De-

vice response at wavelengths shorter than the notch, as seen in Figure 3.1, is forward-dominant, while response at wavelengths longer than the notch position are reverse-dominant. This indicates a "splitting" between efficiencies in this voltage range, which implies that a potential offset in the barrier must be present.

Assuming the simplified model of two emitters separated by a single barrier is valid, current directionality will be affected by barrier profile. The emission efficiency is determined by the effective workfunction only, so which ever emission direction has the lowest effective workfunction energy, it will have the highest emission efficiency, at all wavelengths of response. This leaves collection efficiency, which is determined by distance to the barrier maximum. If the reverse effective workfunction is less than the forward effective workfunction, $\Delta_{REV} < \Delta_{FOR}$, then the reverse current direction has greater emission efficiency. In order for part of the response spectrum to be dominated by forward photocurrent (in this case, for wavelengths shorter than the notch), the distance from the interface to the barrier maximum must be shorter in that direction, so that it can be dominant in collection efficiency. This particular configuration of band structure is shown in Figure 3.4(b), and is considered to be the necessary setup for the notch to be present in the response of these detectors.

Calculations were carried out for each applied voltage in which the cancellation is visible in the responsivity spectra. Parameters used in the calculation other than device parameters given earlier are: L_e = 4000 Å, L_p=60 Å which are given by Aslan, et al.[13], in agreement with ranges given by Mooney and Silverman.[10] Scattering length, assumed here to be independent of energy, in the barrier is L_s = 300 Å.[7] The notch in the spectrum is the point where the two current directions cancel each other out, and since the total quantum efficiency is proportional to photocurrent (photoyield), ($\eta_{FOR} \propto i_{FOR}$), the requirement for calculation becomes

$$\eta_{FOR}(\lambda) = \eta_{REV}(\lambda) \tag{3.10}$$

where η_{FOR} (η_{REV}) is the total quantum efficiency calculated in the forward (reverse) direction, and λ is the wavelength at which the notch occurs for the applied bias.

From the inclusion of a potential offset in calculation, it is expected that the GaAs-on-AlGaAs interface, or barrier interface closer to the top contact, will have a larger potential than the AlGaAs-on-GaAs interface, as shown in Figure 3.4b. Comparison of thresholds between the positively and negatively biased conditions show such a threshold shift, with device response shown in Figure 3.5, and result in offsets of ~13, ~21, and ~34 meV for aluminum fractions of x = 0.28, 0.37, and 0.57, respectively. Similar results were found previously[14] by Tsai et. al. in GaAs/AlGaAs QWIPs. They modeled asymmetric dark current by including a potential spike, a potential increase in the barrier with a smaller width compared to the barrier, at the GaAs-on-AlGaAs interface, showing an offset of 2, 9, and 12 meV for aluminum fractions of x = 0.1, 0.15, and 0.26, respectively. Our threshold results show the similar increase in barrier offset with increasing aluminum fraction. While their work modeled a potential spike offset, only due to the discrepancy between calculated and experimental range of applied bias discussed earlier was a linear gradient used as a potential spike would make the shift between current directions even more dramatic. Li et al. explain asymmetry in QWIPs via a graded structure occurring during growth of the device, and suggest that the asymmetry is more pronounced in devices grown via MBE, the growth method used for the split-off detectors, than in Metal-Organic Chemical Vapor Deposition (MOCVD).[15]

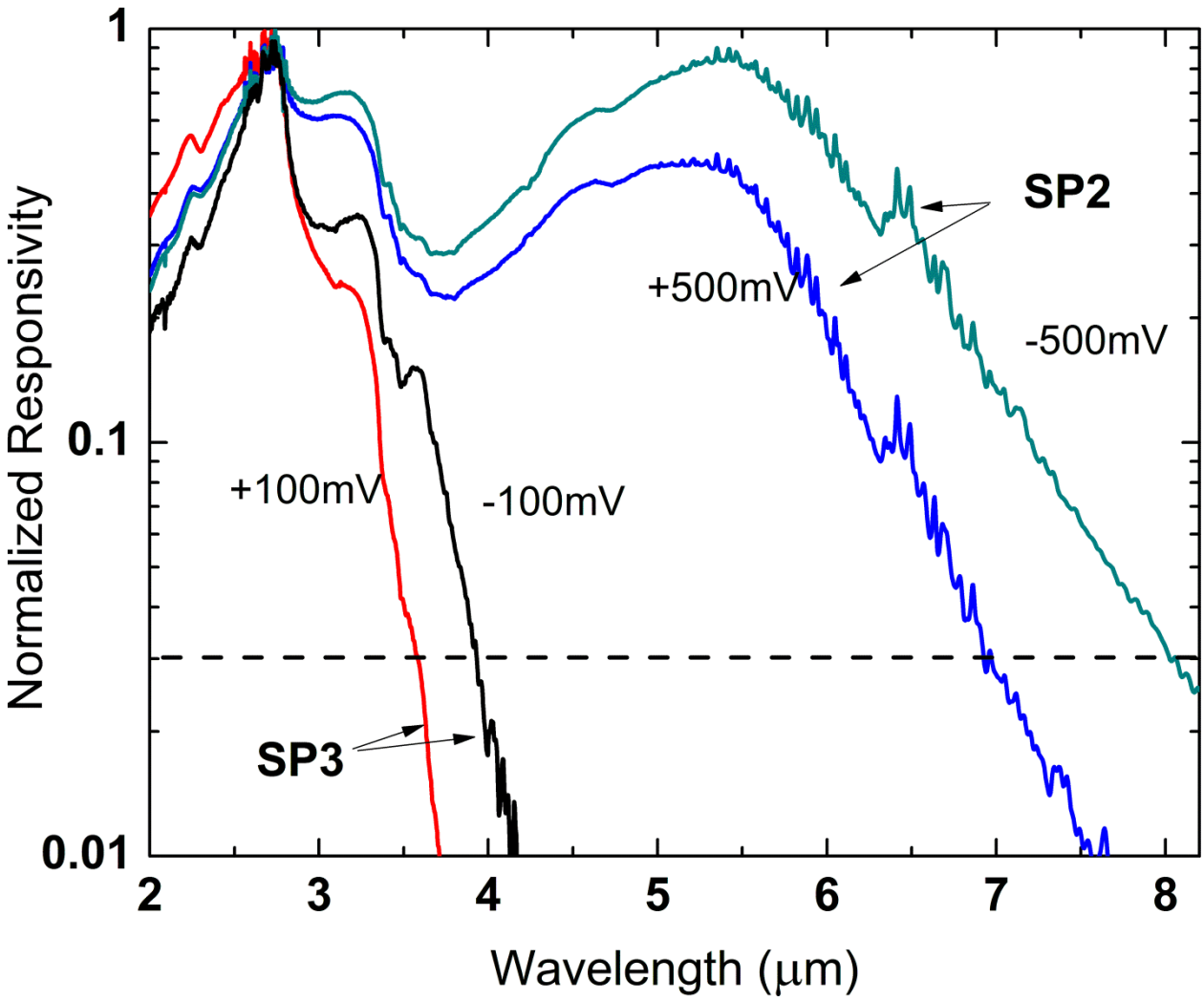

Figure 3.5: Normalized Responsivity of SP2 and SP3 showing threshold differences between negative and positive applied bias. Calculated threshold wavelength was located for the device, then a horizontal line drawn to the other bias curve, to measure the separation.

Using these potential offsets, calculations were performed by matching the notch position from experimental data. The results for two notch positions in SP2 are shown in Figure 3.6. It can be seen that the bias used in the calculations to match the notch position is larger than the bias used in experiment. One reason is possibly due to the assumption of linear electric field distribution in the calculations. A non-linear field distribution has been shown to occur in studies with QWIPs, with increased non-linearity occurring while under illumination and lower applied bias,[16] which should have an impact in modeling given the low applied voltage. The majority of the electric field is distributed toward the top of the device, resulting in a very large field in the first few barriers, followed by a much lower field in the remaining parts of the device while maintaining an average field through the device of the applied voltage.

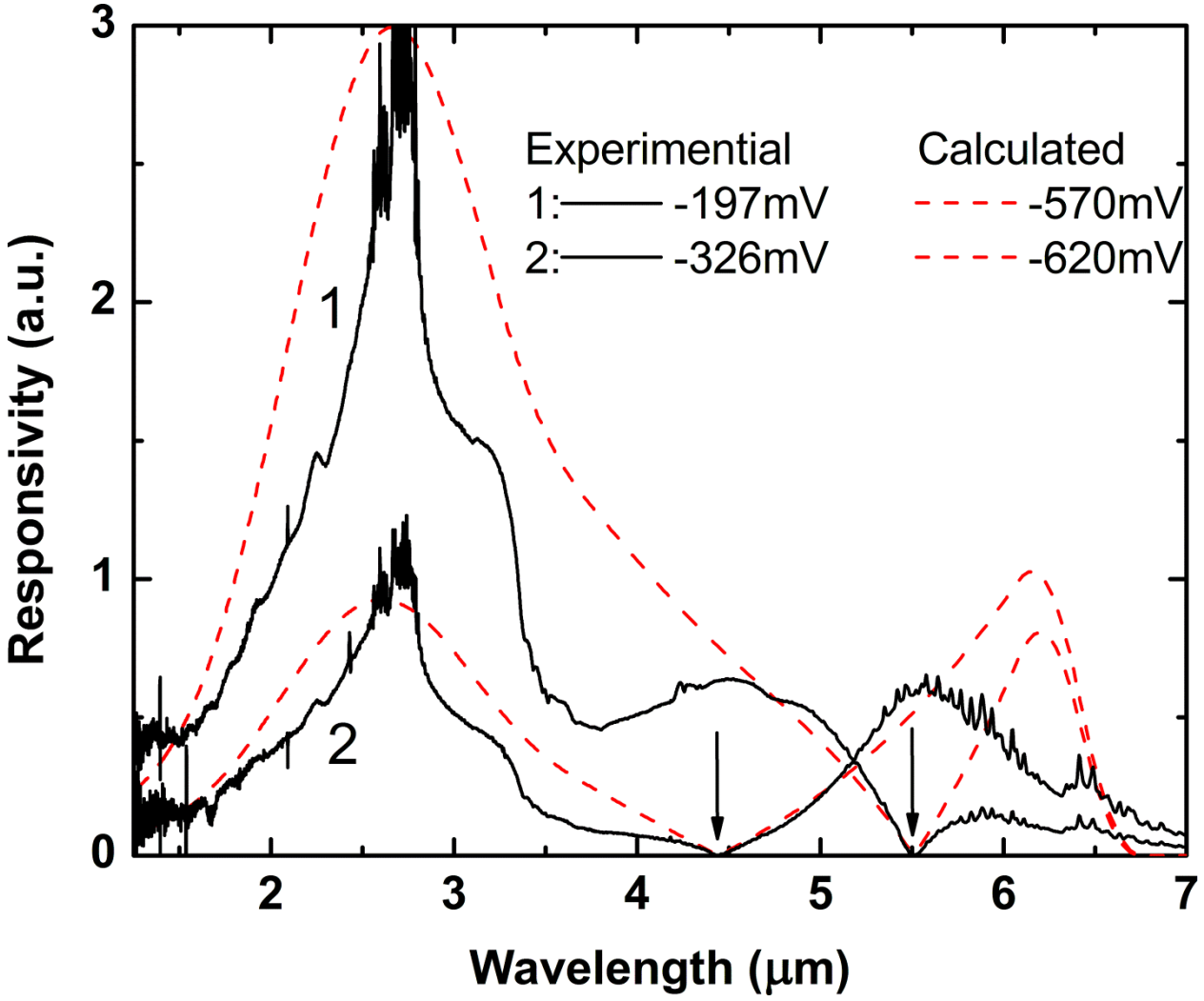

Figure 3.6: Comparison of experimental and calculated response spectra for the SP2 detector at two bias voltages. Using a barrier gradient offset calculated from threshold comparison, electric field was adjusted in calculation to match the notch position. Long wavelength discrepancy in spectral magnitude is the result of an approximation used in the thermalization series truncation.

3.3 Effect of Load Resistance

It should be noted that there is a relation between notch position and the load resistance in the external bias circuit. The higher the load resistance in the circuit, the closer to zero bias the notch occurs. Also at higher load resistance, the range of applied bias in which the cancellation occurs in the spectral response curve is shortened, as is shown for the detectors in Figure 3.7. If the calculations are off because the electric field is not evenly distributed throughout the detector, the dependence on external resistance suggests that for any given average bias field across the detector, the localized electric field will differ depending on the external circuit resistance. It was suggested that perhaps the external resistance was limiting the injection current at the detector contacts, which would have an effect on field distribution, but given that the dynamic resistance of SP2 at 80K is orders of magnitude higher than the highest external resistance tested, the effect should be negligible between the four resistances tested. To test another possibility, time response should be calculated for the detectors.

3.3.1 RC Limited Response

If a detector's response time is slower than that of an incoming modulated signal, responsivity will be reduced. Response times for the detector can be calculated and compared with the modulation frequency of the FTIR signal to see if this is the case.

The electrical frequency for a given wavelength of an FTIR modulated light source is given as:

$$f = v_{OPD} \times k \tag{3.11}$$

where f is the electrical frequency in Hz, v_{OPD} is the optical path difference (OPD) velocity in cm/s, and k is the wavenumber in cm^{-1}. SP1 has the largest wavelength range of the three, from 1.25 µm to 8.50 µm which corresponds to a wavenumber range of 8000 cm^{-1} to 1176 cm^{-1}. The

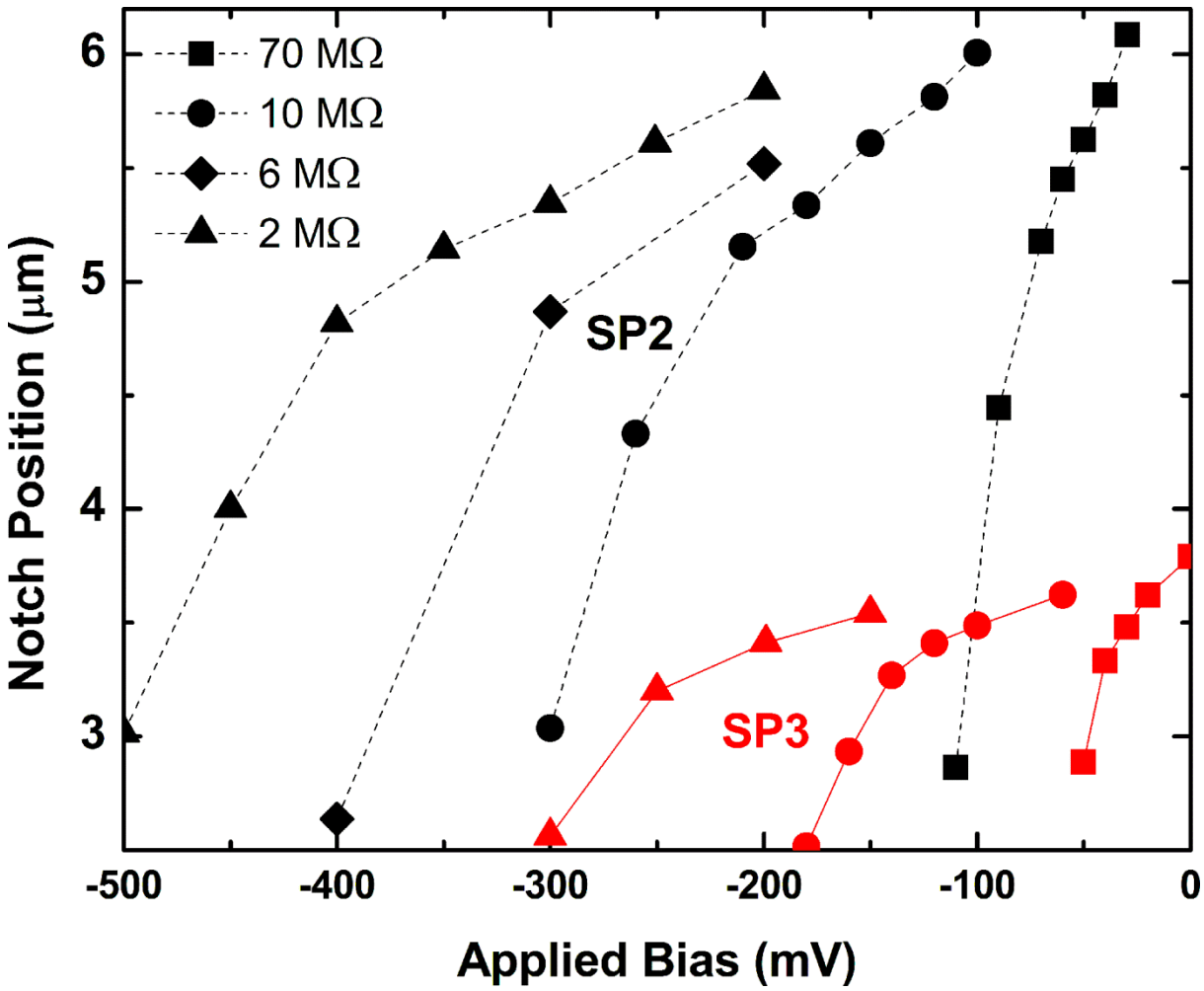

Figure 3.7: Dependence of photocurrent cancellation notch position on the experimental applied bias. Results for SP2 and SP3 for different external circuit load resistors. External resistors are 2, 6, 10, and 70 MOhm.

slowest OPD velocity of the Perkin Elmer System 2000 is 0.05 cm/s, which corresponds to a frequency range of 400 Hz to 60 Hz. SP2 would operate from 400 Hz to 75 Hz, and SP3 would operate from 400 Hz to 112 Hz.

The transit time is the speed with which a carrier can travel through a detector given an electric field-dependent carrier velocity. At high field, velocity becomes saturated, however, the effect we are studying occurs at low bias, and is below the field requirements for velocity saturation. Transit time is given as:

$$\tau_{tr} = \frac{d}{\mu_h E} \tag{3.12}$$

where *d* is the distance the carrier must travel, μ_h is the hole mobility, and *E* is the electric field. Given a hole mobility of 60 cm^2/Vs for GaAs, we arrive at a transit time of τ_{tr} =4.4 ns for a +0.01 V applied bias. Frequency is then:

$$f = \frac{1}{2\pi\tau} \tag{3.13}$$

which gives a transit frequency of ~36 MHz. This is much faster than the FTIR modulated signal, so it isn't limiting response in this region.

Another speed limiting factor is the RC time constant which depends on the detector and circuit's capacitance and resistance:

$$\tau_{RC} = R_{TOT}C = \frac{R_D R_L}{R_D + R_L} C \tag{3.14}$$

where R_D is the detector's dynamic resistance, R_L is load resistance, and C is the detector capacitance. Detector capacitance can be calculated via the parallel-plate capacitor approximation for low frequencies. Capacitance for a single layer would then become:

$$C = \frac{\epsilon \cdot \epsilon_0 \cdot A}{d} \tag{3.15}$$

where ϵ is the static dielectric constant of the material, ϵ_0 is free permittivity , A is the area of the layer, and d is the depth of the layer. From Ioffe, GaAs has a static dielectric constant of 12.37 at 77K, and $Al_xGa_{1-x}As$ has a static dielectric constant of $\epsilon(x)$= 12.90 -2.84x where x is the aluminum fraction.

For SP2, capacitance of the detector is 6.5 pF, and R_D is 4.5×10^9 Ω at 77K. Using a load resistance of 70 MΩ, the RC time constant becomes τ_{RC}=4.14 x 10^{-4} s, which results in a frequency limit of 380 Hz. This is in the response range the detector needs to operate in, and does not include circuit capacitance, which will only slow the response further. The effect is even more pronounced in SP3, which has a higher device resistance. A comparison of responsivity for different load resistances used with SP2 is shown in Figure 3.8. The results for the 6, 10, and 70 MΩ resistors were taken as a percentage of the highest response load resistance (2 MΩ) and compared in Figure 3.9. It can be seen that at shorter wavelengths the response is attenuated more, supporting the theory of RC-limited response as shorter wavelengths correspond to faster modulated signal frequency.

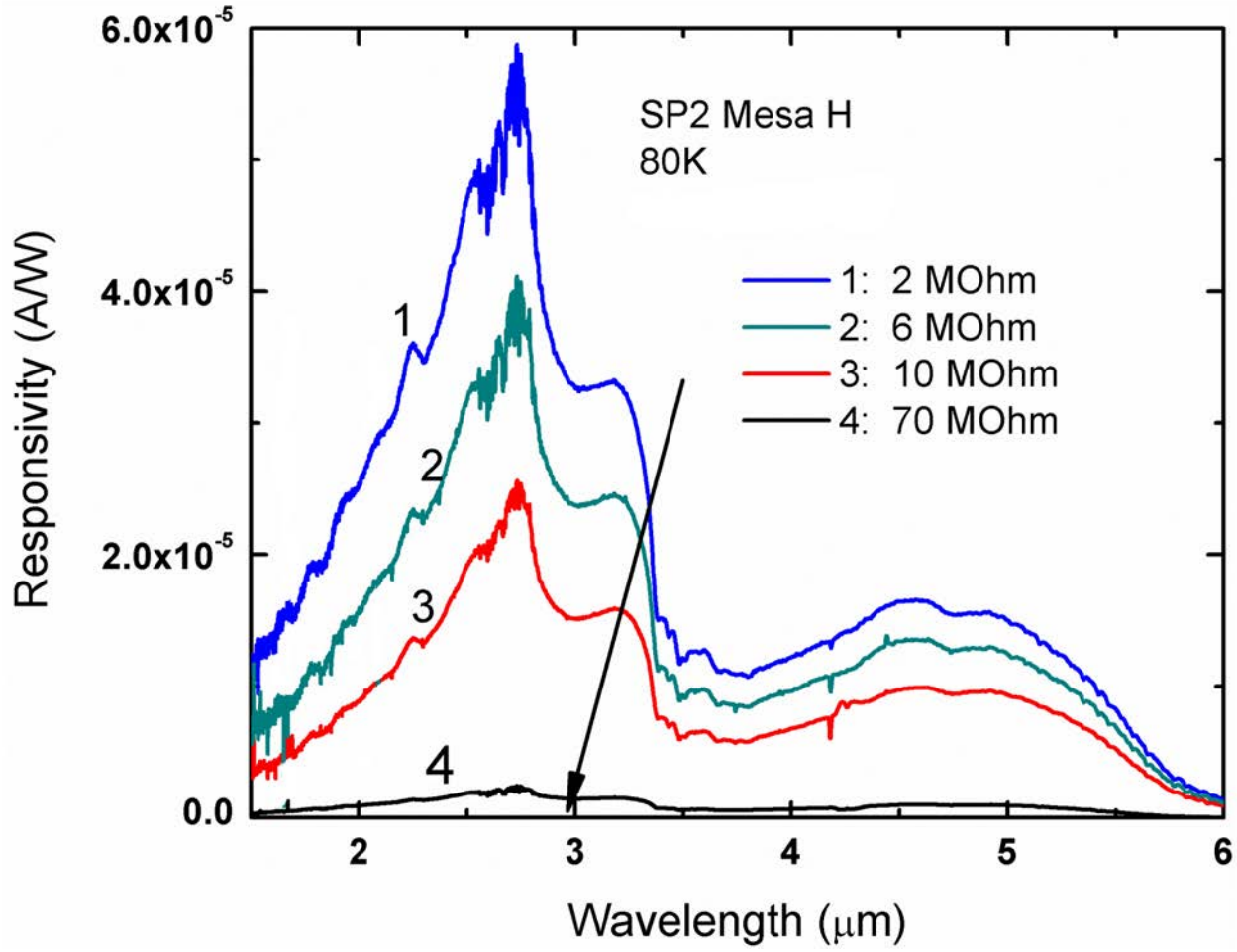

Figure 3.8: Comparison of SP2 responsivity for different load resistors at 80K. Responsivity decreases with increasing load resistance, showing that the detector is RC-limited in its response.

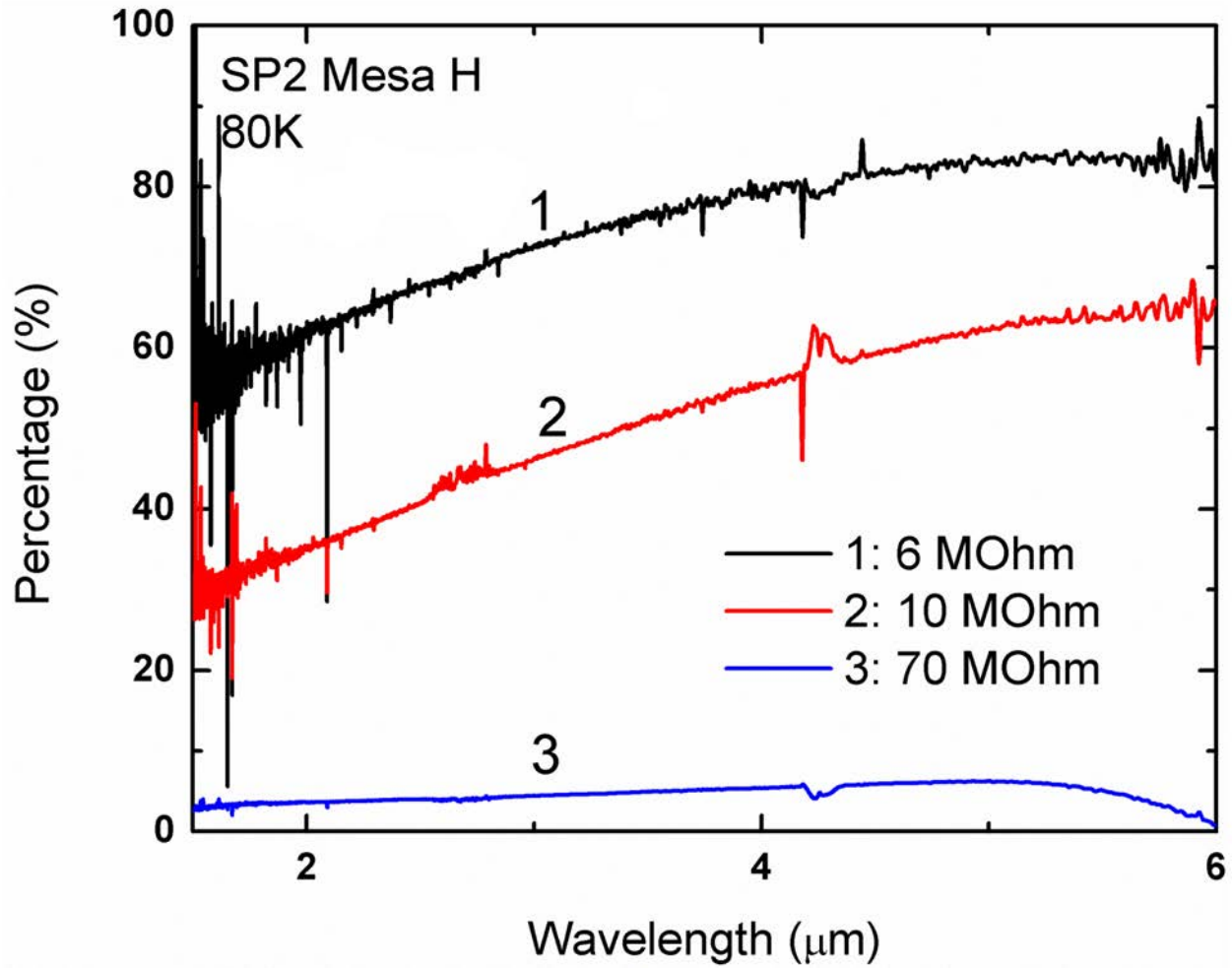

Figure 3.9: Comparison of SP2 responsivity for different load resistors as a percentage of the 2 MΩ response. Because resistance has an effect on the responsivity, the detectors are operating slower than the modulated signal of the FTIR. Further evidence of RC time limiting is that longer wavelengths show higher percentage response because they are slower frequencies.

3.4 Corrections to Photoemission Calculations

Due to the fact that SP2 and SP3 were RC-limited in their response, it became clear that they would not be as useful for modeling efforts, as the experimental results would not accurately represent the notch position as a function of applied bias. Using a lower load resistor could help with the RC-limited response, however a lower load resistor would only increase noise further. SP1 could be used, however, as it operates fast enough to get a real result. SP2 and SP3 were the focus of study before their limitations were understood as they had better responsivity under the experimental conditions of 80K temperature and low-bias. In order to improve the calculations, data from the SP1 detector would have to be used.

The first correction to the model was eliminating the contribution to forward photocurrent from the top contact of the detector. This is because the top contact is etched away down to the first barrier, leaving only the material directly under the gold electrical contacts- the majority of the material is etched, and leaves an optical "window" to the active layers of the detector. This helps the theoretical notch position come closer to experimental by removing a portion of the forward photocurrent.

3.4.1 Multi-layer Effects

One of the most important improvements to the model was including attenuation due to multi-layer effects in the device. Previous papers on photoemission only seemed to address this in terms of the absorption efficiency via multiple reflections at different surface interfaces. To simulate the effect of multiple layers, the collection efficiency, η_C, which is the probability of a charge carrier, once excited from an emitter, to pass through the barrier layer without scattering, is cumulatively multiplied to the absorption and emission efficiencies, depending on how many barriers must be traversed between the original emitter and the top or bottom contacts. A diagram

of this effect in the device is shown in Figure 3.10. The calculation is as follows: each active layer (emitter, bottom and top contacts) has an emission efficiency, η_E , and an absorption efficiency, η_A , which were discussed more extensively in Section 3.2. These two efficiencies are localized to the emitting layer in which the carrier is produced. The collection efficiency deals with the probability of making it through the barrier to be collected. To simplify calculation, only the addition of multiple collection efficiencies was taken into account, and not additional scattering or recombination in the active layers. Each emitter adds to the photocurrent via the absorption and emission efficiency, which is then attenuated by each subsequent barrier the excited carrier must pass through in order to reach the contact layers and contribute to the photocurrent. As can be seen in Figure 3.10, the contributions to the photocurrent in a particular direction (reverse in this example) by each emitter are added together,

$$\eta_{REVERSE} = \eta_2\eta_C + \eta_3\eta_C^2 + \eta_4\eta_C^3 + \eta_5\eta_C^4 + \eta_6\eta_C^5 \tag{3.16}$$

where η_N is the combined absorption and emission efficiencies of a particular emitter, with N being the layer number in the device. In the case where emission, absorption, and collection efficiencies do not vary from layer to layer, as is the case for a particular direction, this can be generalized to:

$$\eta_{REVERSE} = \eta_A\eta_E \times \sum_{i=1}^{N} \eta_C^i \tag{3.17}$$

where N is the number of layers in the device contributing to the photocurrent.

The end result is that largest contribution to photocurrent is from active layers near the contacts, as the emitted carriers are more likely to make it to the contacts without scattering. This also greatly improved on the responsivity calculations that were much higher than experimental results.

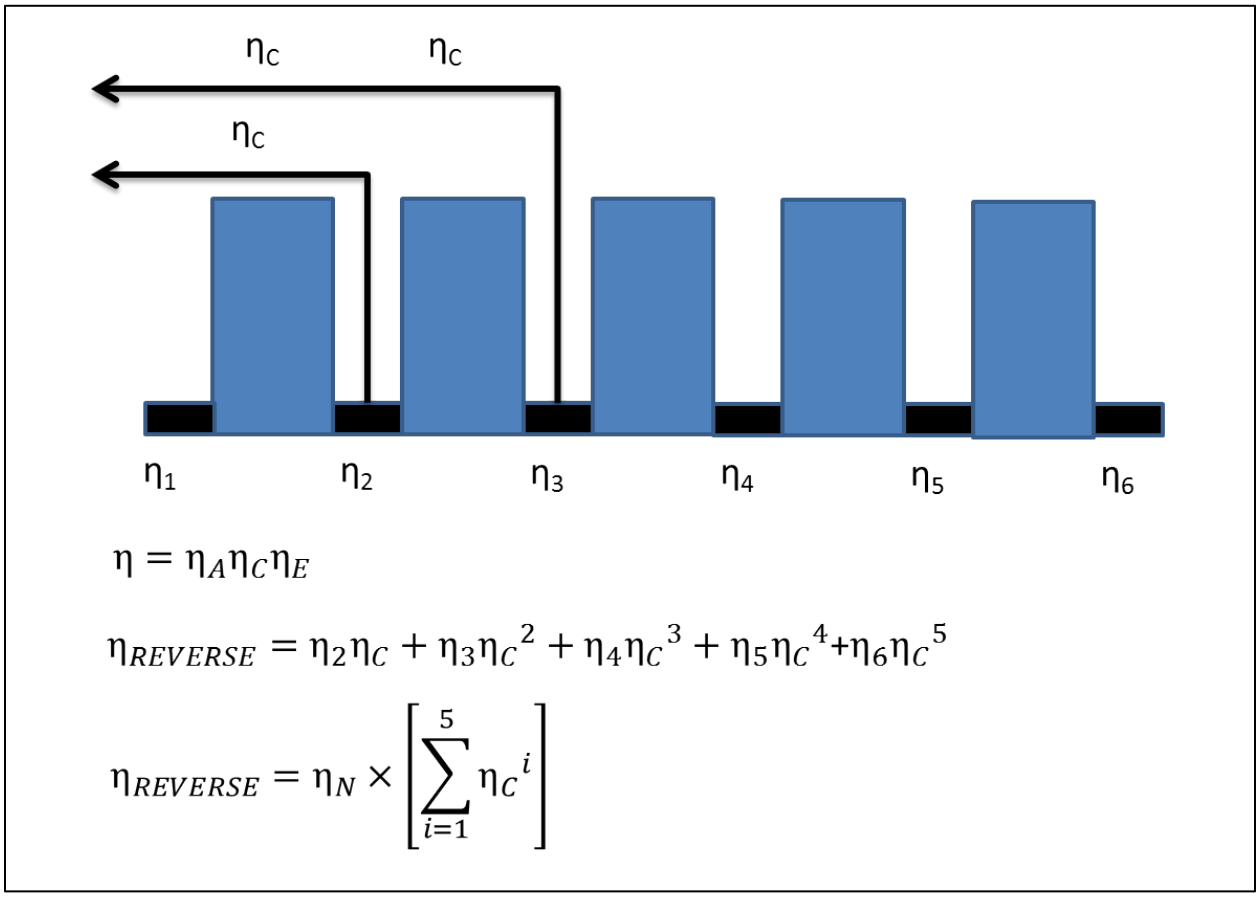

Figure 3.10 Graphical representation of the multilayer effect on overall photoemission. Total quantum efficiency is given as η, and is the product of absorption, collection, and emission efficiencies (η_A, η_C, and η_E, respectively.) The individual emitter efficiencies, η_N, where N is the number of the emitter, is the product of the absorption and emission efficiencies. The number of barriers between the contact layer and the emitter is multiplied to obtain attenuation for emitted carriers based on how many barriers they must travel through. If the field in this region is linear, and all materials remain the same, the end result can be simplified to the equation shown at the bottom (Equation 3.17 in the text.)

3.4.2 Barrier Offset

Finding the correct value for the offset of the potential barrier has been a goal, but has proven difficult. One way to analyze the material composition of the detector, with emphasis on the emitter/barrier interface, would be through Secondary Ion Mass Spectrometry (SIMS) analysis, where an ion beam is projected onto the sample, and ejected secondary ions are analyzed via a mass spectrometer. Unfortunately, this analysis was not performed on the detectors, and as it is a destructive measurement, it is not a desirable method for a finished product that is currently in use for other experiments. Other methods would have to be attempted in order to come up with a value.

First, it should be noted that calculations were carried out in order to see if a non-linear field distribution in the device could account for the notch and subsequent directional preference in the device. These calculations, while not exhaustive, seem to indicate that even with a non-linear field throughout the device, a barrier offset would still be required in order to obtain the photocurrent directionality witnessed in the detector, and subsequent notch seen in spectral response. Any amount of applied field and difference between localized fields would give a single preferred direction, unless one localized field was of the opposite polarity, which has not been suggested in the literature.

As previously stated, early threshold comparisons via responsivity measurements gave a barrier offset of approximately 13 meV. This seemed to be in agreement with the paper on QWIPs by Tsai, et al,[14] but I was not confident in the method for determining it. First, selecting the threshold levels for the responsivity curve seemed arbitrary, as did the bias voltages for comparison, i.e. -100 mV and +100 mV, or -400 mV and +400 mV. This is particularly problematic when taking into account a non-linear electric field in the device. If the field were uniform

throughout the device, comparing two applied biases of opposite polarity could produce useful results because the barrier profile would be uniformly affected, just in opposite directions. If there is an offset in the barriers, then one would expect the detector under negative bias to have a lower threshold energy than that of the equivalent positive bias, as explained in Section 3.2. Because field non-linearity is more pronounced under lower average field conditions,[17] a spectral threshold comparison was done at ±1V for SP1, with results shown in Figure 3.11. Thresholds were compared by measuring the responsivity of the device under the particular bias, followed by multiple measurements of the detector noise by shielding the detector from incoming light, under otherwise matching experimental conditions. The "dark" operating condition provides a "noise floor" to determine where the threshold is located.

As previously shown, when comparing the calibrated spectra between opposite field polarities, the device under negative bias always has a response at longer wavelengths than the device under positive bias (Figure 3.11a). This is true between all three detectors, and at all bias levels that have been measured (except for bias levels where the notch is interfering with the long wavelength response, which is to be expected.) However, when the thresholds are determined by the individual noise floors, as shown in Figure 3.11 (b and c), a different picture seems to emerge. It can clearly be seen that the noise levels under dark conditions for the -1V bias measurements are much higher than under positive bias. While this would seem to suggest that the threshold energy is lower for the device under positively biased operation, I do not feel this is necessarily the case, given the amount of supporting evidence for a lower threshold under negative bias: (i) previous studies support the conclusion of unequal interface energy levels, (ii) it is thus far required to explain this directionality and notch, and (iii) direct comparison between polarities suggest lower thresholds occur under negative bias.

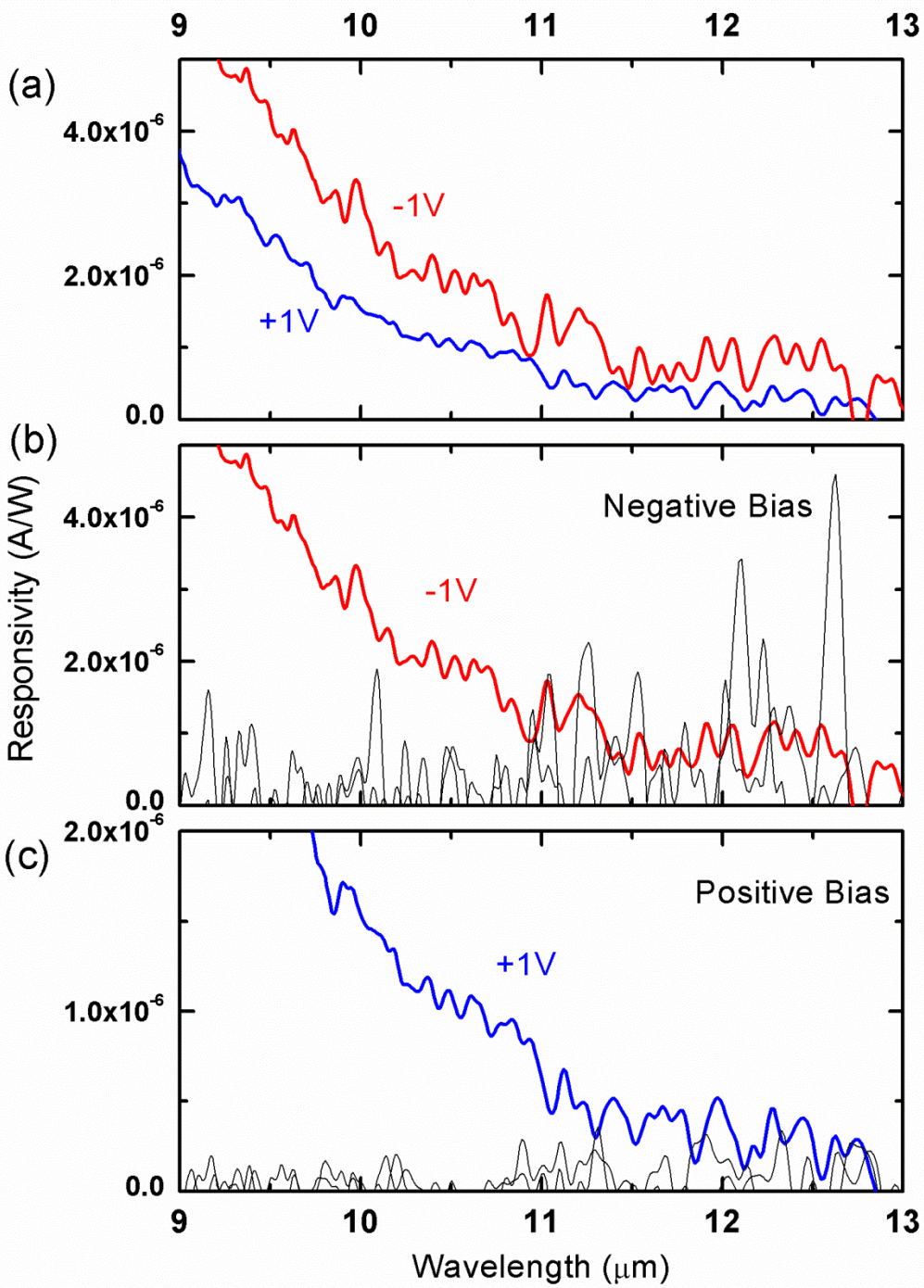

Figure 3.11 Comparison of spectral thresholds under positive and negative bias. A comparison between the two bias polarities is shown in order to attempt to find the barrier offset of the AlGaAs barriers. Direct comparison of the calibrated responsivities (a) show clearly that negative bias has a lower energy threshold (longer wavelength) than that of positive bias.

It is not clear why the device is so much noisier under negative, but given the previously mentioned reasons, I do not believe a spectral comparison which uses the noise floor as the determining factor for threshold energy is a clear contradiction of previous findings. It is should also be noted, that while the noise of the responsivity spectrum is greater for negative bias, it is not nearly as big of a difference between noise levels under dark conditions. One would expect these to be consistent between the two, but this does not appear to be the case. Even with similar noise floors, the non-linearity of the electrical field could still play a substantial role, even at this higher bias level.

Another method that was decided on was to use Current-Voltage-Temperature (IVT) data to create Arrhenius plots as a function of applied bias, which would give the threshold energy as a function of bias. The results of the IVT / Arrhenius data are plotted in Figure 3.12. Fitting the data linearly, as threshold decreases with increasing bias due to band bending, for both polarities, then taking the difference between y-intercepts gives a difference of ~9 meV, with the negative bias showing a lower threshold. This is lower than the previously found offset of 13 meV found via responsivity threshold polarity comparison, which better fit the projection of increasing barrier offset with aluminum fraction found in the QWIP paper.[14]

Given the difficulty in the methods used to precisely predict the energy level of a barrier offset, it was decided to continue with some uncertainty and test the model further, particularly testing the effects of non-linear field distribution in the device, which have been noted before. To do this, a barrier offset of 10 meV is used. Along with the multi-layer effects, an approximation for non-linear field distribution is used which models after previous papers on the subject.

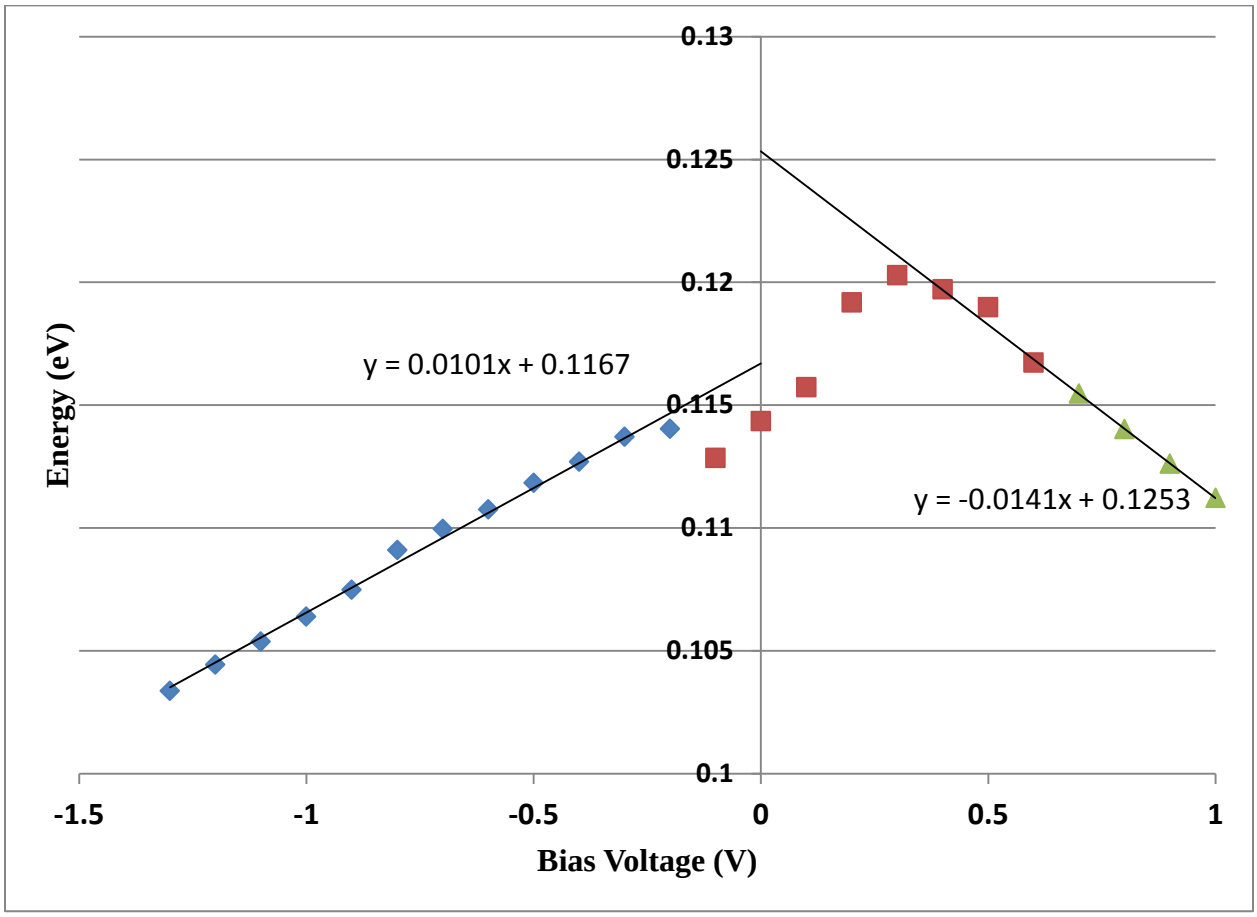

Figure 3.12 Plot of threshold energies for SP1 derived from Arrhenius plots. It was thought that linear fits to the data from either side would show a difference in threshold energy depending on which polarity was chosen. The y-intercept for both would show the difference between the two. Through this method, an offset of 8.6 meV was found.

3.4.3 Non-linear Field Distribution

As stated previously, papers on dark current mechanisms in QWIPs have suggested that the applied electric field in the detector is not evenly distributed.[17] Through self-consistent modeling of dark current, they suggest that the electric field is distributed mostly over a top few barriers of the detector, impacting the top 4 emitters, with a much lower field in the rest of the device, which results in the average field that is measured with bias. This effect was said to be more pronounced, that is, a greater disparity between the largest field near the top of the detector and the low field in the rest of the detector, under (a) lower bias voltages, and (b) under illumination of the detector. Since these conditions both apply to the operating conditions in this study, calculations were carried out to approximate a non-linear field distribution, and its effect on notch position as a function of applied bias.

To approximate this effect, the detector barriers were divided into two groups: (a) the top 5 barriers, which includes the top 4 emitters, and is called the TOP GROUP, and the bottom 26 barriers, 26 barriers, known as the BOTTOM GROUP. The average field of the entire structure was calculated from the applied bias voltage and the field of the two sections was varied while maintaining the same average field throughout the device. As the field of the top group was increased, the field in the bottom group would decrease to maintain the total average. The experimental bias voltages were used to set the average electric field, while the experimental notch position for said bias voltage was the fitting parameter for adjusting the fields between the two barrier groups. The notch was visible in responsivity measurements from V_{BIAS}= -75 mV to -200 mV, with data points taken at 25 mV intervals. Since it was decided to use 10 meV as a barrier offset, the only fitting parameter was the localized electric field.

Using the average electric field and corresponding notch position from experimental results, calculations were carried out to find if the localized electric fields of the top and bottom groups could match the notch position. Unlike the original calculations that placed the bias at much larger levels than found experimentally, the new model, which includes multi-layer and non-linear field distribution approximations, was able to properly match experimental results. The Top Group of barriers/emitters are under a much larger localized electric field than the rest of the device (the Bottom Group.) For instance, an applied bias of -150 mV has an average electric field of -0.806 kV/cm, the bottom group localized field is -0.438 kV/cm, while the top group localized field is -2.62 kV/cm; which is approximately six times larger than the bottom group's field. At each field value, the barrier profile was calculated for both groups in order to determine the necessary values for calculation of photoemission: valence band offset, and barrier maximum position which in turn determines the collection efficiency, each of which is calculated for both the forward and reverse directions. The calculated single barrier profiles for the top and bottom group solutions for an applied bias of -150 mV are shown in Figure 3.13. The barrier on the left, 3.13(a), is the profile for the top five barriers, with an electric field of -2.62 kV/cm. The barrier on the right, 3.13(b), is the calculated profile for a single barrier of the bottom group (26 barriers), with a field of -0.438 kV/cm. As one can see, the barrier maximum, x_m , moves to the right as the field is increased. This results in higher collection efficiency for the reverse photocurrent direction (from bottom contact toward top contact), as well as a lower threshold in that direction, which increases the emission efficiency as well. This is why at high negative bias, the photocurrent flows in the negative direction, and at high positive bias, it flows in the positive direction (toward the bottom contact.) Results for the different field distributions are shown in Table 3.1.

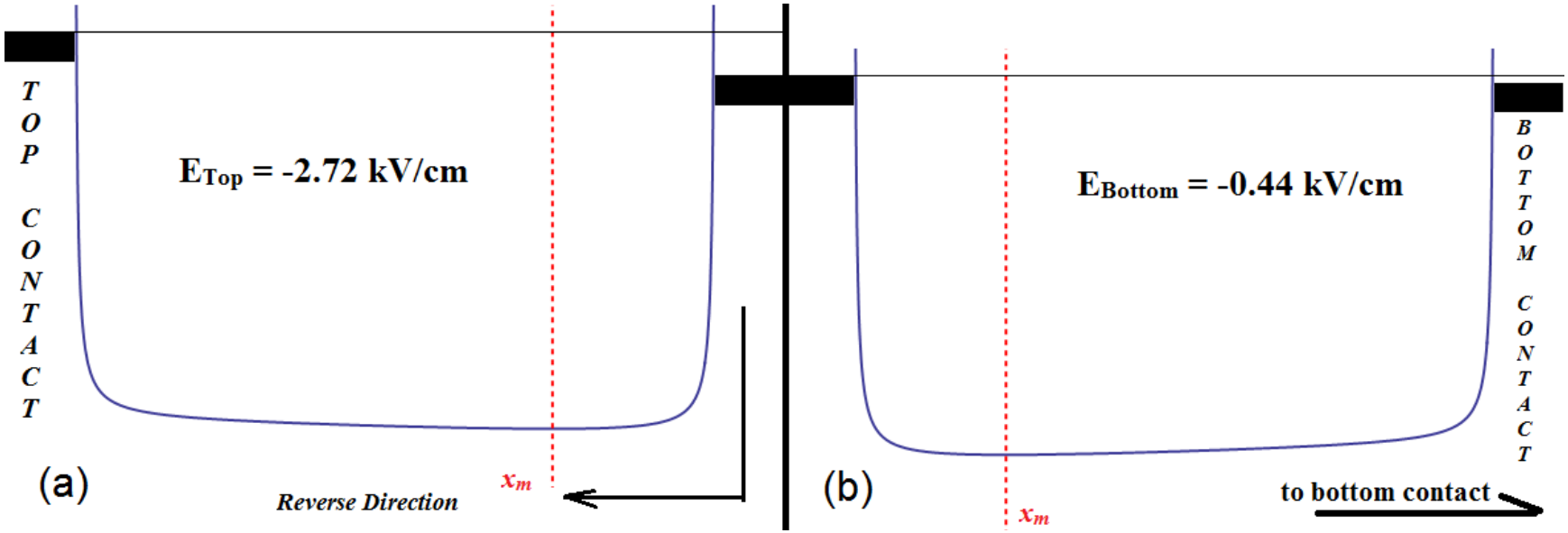

Figure 3.13 Single barrier profiles calculated for an applied bias of -150 mV for the SP1 detector. This voltage gives an average electric field of -0.806 kV/cm in the device, which is not evenly distributed throughout. The majority of the field is concentrated in the first 5 barriers (a) referred to as the Top Group. The rest is distributed throughout the rest of the device, called the Bottom Group (b), which consists of the bottom 26 barriers. Because the field is distributed over 26 barriers instead of 5, the field in the Bottom Group (b), is much lower than in the Top Group (a). The red dotted vertical line represents the barrier maximum, x_m , and determines the interfacial workfunction energy, as well as the collection efficiency- the closer the maximum is to an interface, the less the chance of scattering for an emitted carrier from that interface. As a result, for the Top Group, photocurrent travelling toward the top contact (reverse direction) is dominant, while for the Bottom Group, current traveling toward the bottom contact (forward direction) is dominant.

Table 3.1. Results for non-linear field distribution calculations given a barrier offset of 10 meV. Calculated values are divided between the two sections of the device, the TOP SECTION (Top 5 Barriers / 4 Emitters) and the BOTTOM SECTION (Bottom 26 Barriers / 26 Emitters). The right side of the table shows the experimental notch position which was used as the fitting parameter for the model. The Local Field, which was adjusted to match experimental notch position, is given for each section. It can be seen that the Top Section has a much higher localized field than the Bottom Section, and that the difference between localized fields decreases as bias is increased. This is in agreement with previous work published on QWIP current mechanisms. The Barrier Workfunction and Collection Efficiency give the relevant values obtained by using the particular localized fields.

Applied Bias	Average Electric Field	TOP SECTION				BOTTOM SECTION			Notch Position
		Local Field	Current Direction	Barrier Workfunction	Collection Efficiency	Collection Efficiency	Barrier Workfunction	Local Field	
(mV)	(kV/cm)	(kV/cm)		(meV)	(%)	(%)	(meV)	(kV/cm)	(μm)
-75	-0.403	-2	FORWARD	145.4	28.9	65.3	141.3	-0.096	8.06
			REVERSE	133.4	46.8	20.7	140.8		
-100	-0.538	-2.55	FORWARD	147.6	23.4	64.9	141.4	-0.151	7.46
			REVERSE	132.3	57.9	20.9	140.5		
-125	-0.672	-2.72	FORWARD	148.4	22.5	63.7	141.6	-0.278	6.96
			REVERSE	132.1	60.2	21.2	139.9		
-150	-0.806	-2.72	FORWARD	148.4	22.5	62.2	141.8	-0.438	6.52
			REVERSE	132.1	60.2	21.8	139.2		
-175	-0.941	-2.88	FORWARD	149.1	21.8	60.7	142.0	-0.567	5.17
			REVERSE	131.8	62.1	22.3	138.6		
-200	-1.075	-2.82	FORWARD	148.8	22.1	58.5	142.3	-0.740	3.18
			REVERSE	131.9	61.3	23.1	137.8		

From the field results shown in Table 3.1, one can see that as the bias increases, the fields of both groups increase, however the localized field for the top group begins to level off, with the bottom group continuing to increase. This would indicate that as the overall field is increased, the difference between the localized fields becomes less and less; that is, it is becoming more linearly distributed. This is in agreement with the QWIP paper which discussed field non-linearity in the device- they found as bias increases, so too does field linearity.[17] A comparison of the field strengths as a function of applied bias is shown in Figure 3.14. The percentage difference between the fields of the top and bottom groups can be seen in Figure 3.13(b) which shows the decrease in percentage difference as bias is increased indicating increased linearity.

Due to the multilayer effects, the majority of the photocurrent comes from the emitters closest to the contact layers, as the more barriers between any particular emitter and a contact the more the signal is attenuated. In the final model, there are 5 components to the net photocurrent: the top group, forward and reverse directions, the bottom group, with forward and reverse directions, and the bottom contact, which would only contribute to the reverse direction (emission from the bottom contact toward the top contact.) However, only two of these contributions are large enough to have a major impact. The top group in the reverse direction and the bottom group in the forward direction are the dominant contributors to photocurrent, as they are the closest active layers with directionality close to the contact. Of the bottom group with forward directional photocurrent, only the closest emitters to the bottom contact will contribute—emitters closer to the top of the device are too far from the bottom contact and will be attenuated. A log plot of the individual contributions is shown in Figure 3.15(b). The third largest contribution comes from the reverse-direction bottom group emitters, as the top most emitters in this group are only separated from the top contact by the top group (5 barriers.) This contribution is still 3

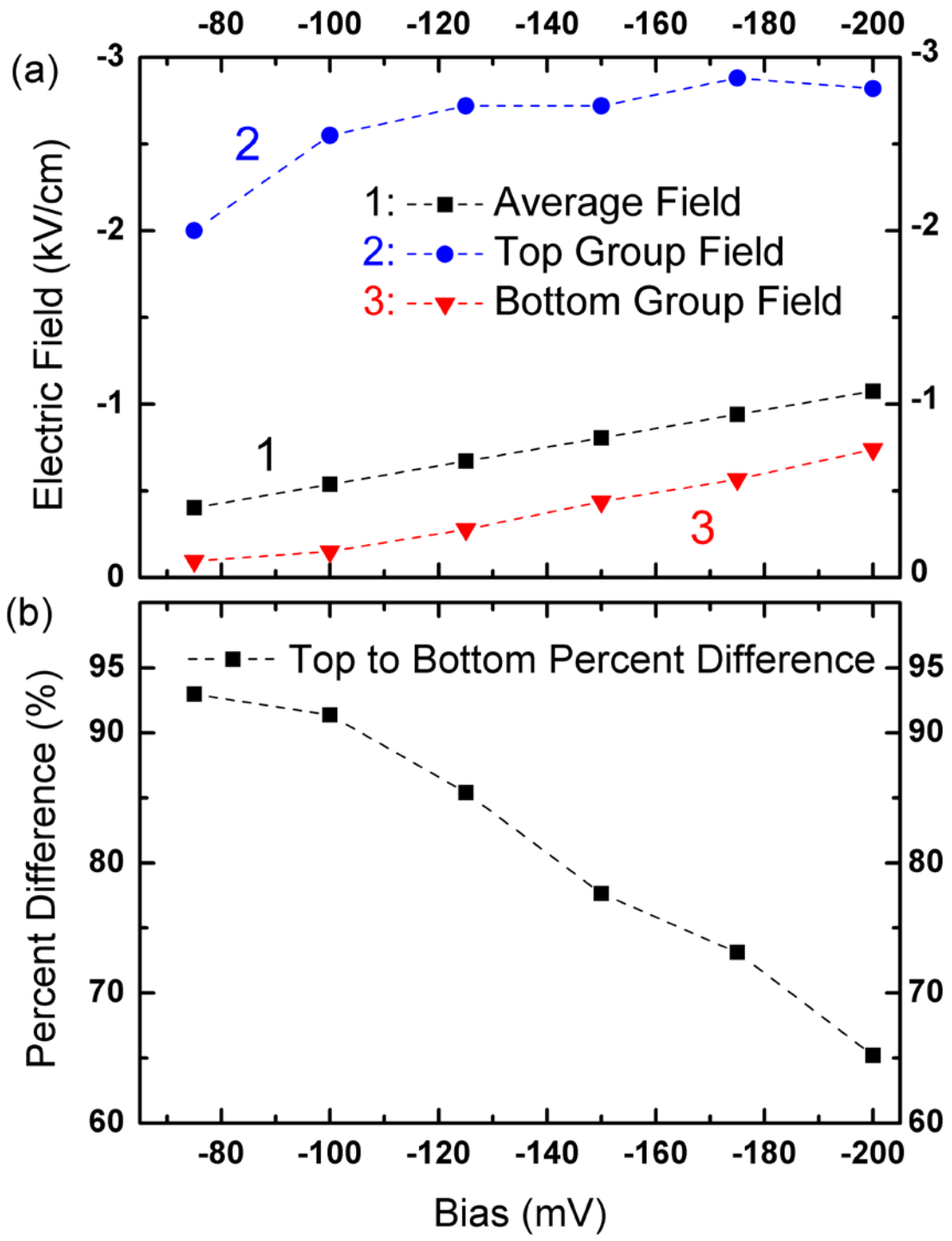

Figure 3.14 The comparison of the electric field distribution in the device. The direct comparison of field strengths between the average, top and bottom groups is shown in the top graph (a). Average and bottom fields continue to increase, while the field in the top of the device begins to level off. The bottom graph (b) shows the percentage difference between the local fields of the top group and the bottom group. This shows a clear decrease in the percentage difference with increasing bias, indicating an increase in the linearity of the field distribution.

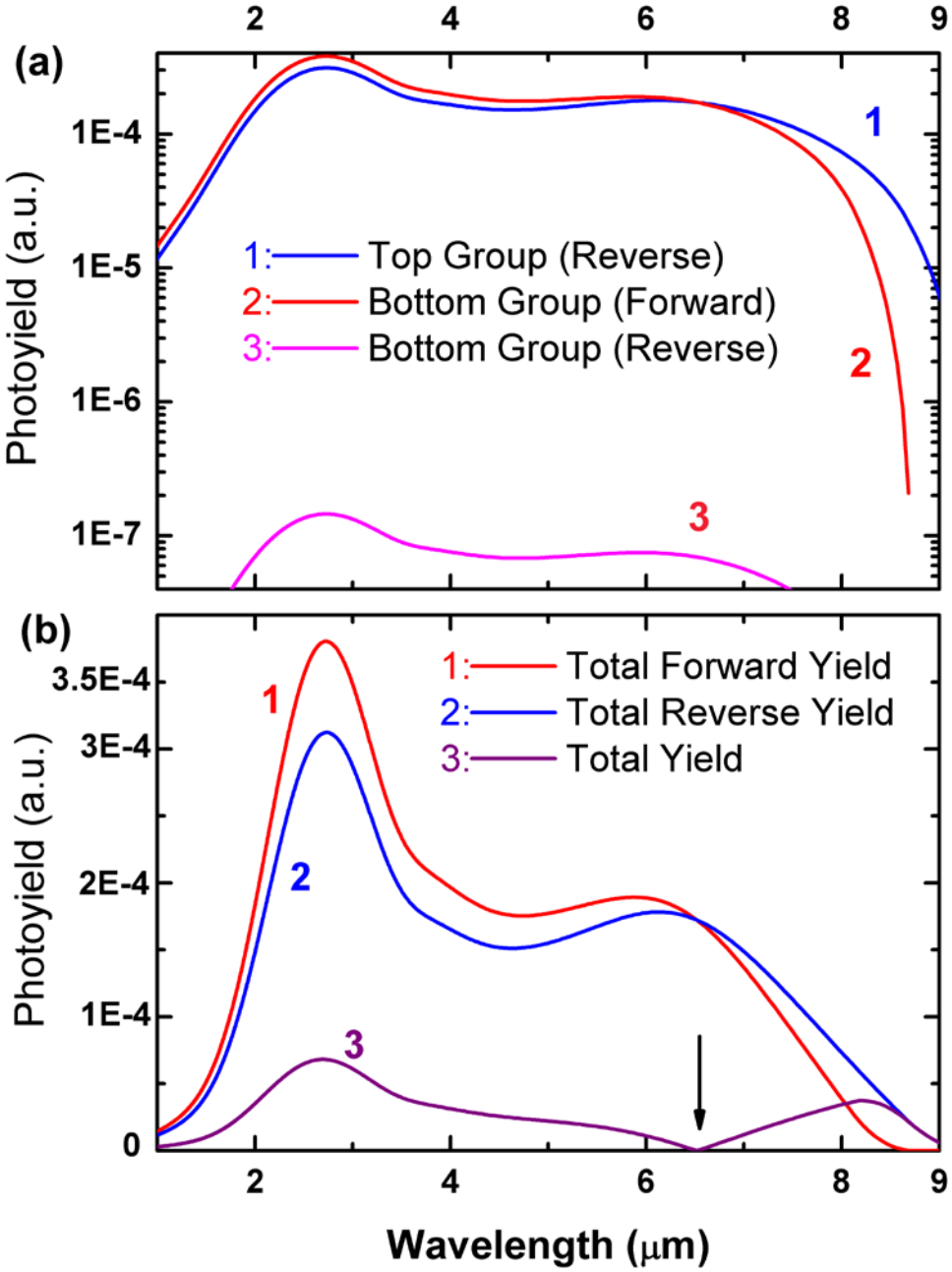

Figure 3.15. Comparison of total photoyields calculated for -0.15 V for the SP1 detector. Individual contributions are compared (a) via log scale to show where forward and reverse directions overlap. Log scale also helps show the shape of the lower yields that the Bottom Group in the Reverse direction give. As it can be seen, the total yields are dominated by reverse-direction photocurrent of the Top Group, and forward-direction photocurrent of the Bottom Group. The next largest contributor is three orders of magnitude lower, and the other two- Top Group (Forward) and Bottom Contact (Reverse) are at least ten orders of magnitude smaller. The total yields for the forward and reverse direction are shown in (b), with the absolute value of the total yield showing the notch in the spectrum.

orders of magnitude lower than the strongest 2 contributors. The two lowest contributions (Top Group Forward direction, and Bottom Contact Reverse direction) are another 10 orders of magnitude weaker, as emitted carriers from these sections would have to travel through most of the device.

3.5 Conclusion

The notch that is observed at low bias in the three split-off band detectors under study is likely due to an offset in the barriers which results in a net forward-directional photocurrent under zero applied bias, aiding in photovoltaic operation. This offset results in a larger potential occurring at the GaAs-on-AlGaAs interface than the AlGaAs-on-GaAs interface of $Al_xGa_{1-x}As$ barriers, which is thought to arise from the epitaxial process during the growth of the device. Such a barrier offset has been discussed in previous studies as a way to describe asymmetrical dark current mechanisms in Quantum Well photodetectors. Calculations were carried out to replicate the effects of bias on the notch, as well as better resolve the parameters of the barrier offset, in hopes of confirming its existence. An initial model was developed based on previous studies involving photoemission processes in photodetectors, and the addition of a potential offset resulted in similar photocurrent cancellation as seen in experiment. Discrepancy in the field required in calculation to that of the experimentally measured field led to a series of improvements to the model to rectify this. Multi-layer effects and non-linear field distributions were both approximated, and resulted in calculations that closely resembled the results seen in experiment. While the value of the potential offset was not precisely determined, partly because of the inability to measure it directly, and partially due to 2 out of 3 of the detectors operating slower than the light modulation of the FTIR, invalidating their usefulness in matching theory to experiment.

SP1, with an aluminum fraction of x=0.28, is likely to have a barrier offset of 10±5 meV, with increasing offsets with increasing aluminum fraction. This value appears to be in agreement with previous studies, and is acceptable when modeling the theoretical output of the detector.

REFERENCES

1. S. P. Mahulikar, H. R. Sonawane and G. Arvind Rao, Progress in Aerospace Sciences **43** (7–8), 218-245 (2007).
2. (Caltech), Vol. 2013.
3. A. Einstein, Ann. Physik **17**, pp-pp (1905).
4. A. G. U. Perera, S. G. Matsik, B. Yaldiz, H. C. Liu, A. Shen, M. Gao, Z. R. Wasilewski and M. Buchanan, Appl. Phys. Lett. **78** (15), 2241-2243 (2001).
5. S. G. Matsik, M. B. M. Rinzan, D. G. Esaev, A. G. U. Perera, H. C. Liu and M. Buchanan, Appl. Phys. Lett. **84** (18), 3435-3437 (2004).
6. Y. F. Lao, P. K. D. D. P. Pitigala, A. G. U. Perera, H. C. Liu, M. Buchanan, Z. R. Wasilewski, K. K. Choi and P. Wijewarnasuriya, Appl. Phys. Lett. **97** (9), 091104-091103 (2010).
7. A. G. U. Perera, H. X. Yuan and M. H. Francombe, J. Appl. Phys. **77** (2), 915-924 (1995).
8. H. X. Yuan and A. G. U. Perera, IEEE Trans. Electron Devices **44**, 2180-2186 (1997).
9. V. E. Vickers, Appl. Opt. **10**, 2190-2192 (1971).
10. J. M. Mooney and J. Silverman, IEEE Trans. Electron Devices **32**, 33-39 (1985).
11. S. G. Matsik, P. V. V. Jayaweera, R. C. Jayasinghe, A. G. U. Perera, K. K. Choi and P. Wijewarnasuriya, J. Appl. Phys. **106**, 1064503 (2009).
12. M. B. Rinzan, S. Matsik and A. G. U. Perera, Infrared Physics & Technology **50** (2-3), 199-205 (2007).
13. B. Aslan and R. Turan, Infrared physics & technology **43** (2), 85-90 (2002).
14. K. L. Tsai, C. P. Lee, K. H. Chang, D. C. Liu, H. R. Chen and J. S. Tsang, Applied Physics Letters **64** (18), 2436-2438 (1994).
15. N. Li, L. Fu, N. Li, Y. C. Chan, W. Lu, S. C. Shen, H. H. Tan and C. Jagadish, Journal of Crystal Growth **222** (4), 786-790 (2001).
16. M. Ershov and V. Ryzhii, Appl. Phys. Lett. **67**, pp-pp (1995).
17. L. Thibaudeau, P. Bois and J. Y. Duboz, Journal of Applied Physics **79** (1), 446-454 (1996).

APPENDICES

Appendix A Mathematica Code

```
ClearAll["Global`*"]
biasvoltage=-.15;
fieldA=-272000;
fieldB=-43846;



barrierwidth=6*^-8;
valbo=.14610;
activefermi=0.0111;
contactfermi=.031;
(*name="c:\output\apr9_yield\April9_sp3_ttlcurrent_neg60mV_test_vbopt28589.csv";*)

escat=.002; (*Energy lost per collision. In Aslan's paper between 1 and 5 meV*)
lp=60;(*Mean free path between semi-elastic collisions. Given as 60 Angstrom *)
le=4000;(*Mean free path between collisions with cold electrons. Given as 4000 Angstrom*)
lstar=N[(le*lp)/(le+lp)]; (*Lstar. 1 / lstar = 1 / le  +  1 / lp*)
γ=N[le/(le+lp)];

workfunction[bias_,fermi_,option_,graph_,biasFieldAverage_,numbarriers_]:=Module[{q=-
1.602176*^-19 ,∈naught=8.8541878*^-12 ,∈s=13,electscat=3*^-
8,ϕbias,ϕmultiple,ϕtotal,xm,threshold,fermiplots,xmline,bandprofile,final,offset,x},
  offset=-.010/barrierwidth;
  (*biasFieldAverage=bias/(31*barrierwidth);*)
  ϕbias[x_]:=q*biasFieldAverage*x;
  ϕmultiple[x_]:=-(q^2*barrierwidth)/(16*Pi*∈naught*∈s*x*(barrierwidth-x));
  ϕtotal[x_]:=valbo +offset*x +( ϕbias[x]+ ϕmultiple[x])*6.24150974*^18;
  xm=Solve[D[ϕtotal[x],x]==0 &&barrierwidth≥ x≥ 0,x];
  threshold=(ϕtotal[x]/. xm)[[1]];

  fermiplots=If[graph=="graph",Graphics[{
     Rectangle[{-2*^-8,0},{0,.0111}],
     Translate[Rectangle[{6*^-8,0},{8*^-8,.0111}],{0,-
(biasFieldAverage*numbarriers*barrierwidth)/numbarriers}]}],0];
  xmline=Graphics[{Red,Dashed,Thick,Line[{{x,-5},{x,5}}/. xm]} ];
  bandprofile=If[graph=="graph",Plot[ϕtotal[x],{x,0,barrierwidth},PlotRange→{-1.5,
1},PlotStyle→Thick],0];
```

```
  final={Which[x==barrierwidth/2,threshold,
     op-
tion=="reverse"&&x<barrierwidth/2,threshold+(biasFieldAverage*numbarriers*barrierwidth)/nu
mbarriers,
     op-
tion=="reverse"&&x>barrierwidth/2,threshold+(biasFieldAverage*numbarriers*barrierwidth)/nu
mbarriers,
     option=="forward"&&x<barrierwidth/2,threshold,
     option=="forward"&&x>barrierwidth/2,threshold]/.xm[[1]],
    Which[
     option=="reverse",N[Exp[-(barrierwidth-x)/electscat]],
     option=="forward",N[Exp[-x/electscat]]
     ]/.xm[[1]],
    If[graph=="graph",Show[bandprofile,fermiplots,xmline,PlotRange→{{-5*^-9,6.5*^-8},{-
0.01,.17}},Axes→ {True,False},Ticks→ None],0],
    x/.xm}

  ]



groupAForwardCalculations=workfunction[biasvoltage,activefermi,"forward",0,fieldA,5];
groupAReverseCalculations=workfunction[biasvoltage,activefermi,"reverse","graph",fieldA,5];
groupBForwardCalculations=workfunction[biasvoltage,activefermi,"forward",0,fieldB,26];
groupBReverseCalculations=workfunction[biasvoltage,activefermi,"reverse","graph",fieldB,26];

bottomContactCalculations=workfunction[biasvoltage,contactfermi,"reverse",0,fieldB,26];


groupArevwf=groupAReverseCalculations[[1]];
groupAforwf=groupAForwardCalculations[[1]];
groupBrevwf=groupBReverseCalculations[[1]];
groupBforwf=groupBForwardCalculations[[1]];
bottomwf=bottomContactCalculations[[1]];


groupAcollectorEfficiencyReverse=groupAReverseCalculations[[2]];
groupAcollectorEfficiencyForward=groupAForwardCalculations[[2]];
groupBcollectorEfficiencyReverse=groupBReverseCalculations[[2]];
groupBcollectorEfficiencyForward=groupBForwardCalculations[[2]];

Print["Group A"]
Print["FORWARD : ",N[groupAforwf*1000,2]," meV  ",N[1.24/groupAforwf,2]," μm
",N[groupAcollectorEfficiencyForward*100,2],"%"]
Print["REVERSE :", N[groupArevwf*1000,2]," meV  ",N[1.24/groupArevwf,2]," μm ",
N[groupAcollectorEfficiencyReverse*100,2],"%"]
```

```
Print["**********************************************************************
**************************"]
Print["Group B"]
Print["FORWARD : ",N[groupBforwf*1000,2]," meV  ",N[1.24/groupBforwf,2]," μm
",N[groupBcollectorEfficiencyForward*100,2],"%"]
Print["REVERSE :", N[groupBrevwf*1000,2]," meV  ",N[1.24/groupBrevwf,2]," μm ",
N[groupBcollectorEfficiencyReverse*100,2],"%"]

Print["**********************************************************************
**************************"]

Print["Results for a SP1 detector at 80K, at ",biasvoltage,"V bias"]
Print["Energy lost per collision :",escat,"eV"]
Print["Lp: Mean free path between semi-elastic collisions. Given as: ",lp," Angstrom"]
Print["Le: Mean free path between collisions with cold electrons. Given as: ",le," Angstrom"]
Print["**********************************************************************
**************************"]
Print["Thresholds: "]
Print["**********************************************************************
**************************"]
groupAReverseCalculations[[3]]  (*PRINTS GRAPH*)
Print["Group A"]
Print["Active Layer (reverse current) :",1.24/groupArevwf," μm  ",groupArevwf," eV"]
Print["Active Layer (forward current) : ",1.24/groupAforwf," μm  ",groupAforwf," eV"]
Print["Collector Efficiency in the Reverse direction
:",groupAcollectorEfficiencyReverse*100,"%"]
Print["Collector Efficiency in the Forward direction
:",groupAcollectorEfficiencyForward*100,"%"]
Print["**********************************************************************
**************************"]
groupBReverseCalculations[[3]]  (*PRINTS GRAPH*)
Print["Bottom Contact (reverse current) :",1.24/bottomwf," μm  ",bottomwf," eV"]
Print["Active Layer (reverse current) :",1.24/groupBrevwf," μm  ",groupBrevwf," eV"]
Print["Active Layer (forward current) : ",1.24/groupBforwf," μm  ",groupBforwf," eV"]
Print["Collector Efficiency in the Reverse direction
:",groupBcollectorEfficiencyReverse*100,"%"]
Print["Collector Efficiency in the Forward direction
:",groupBcollectorEfficiencyForward*100,"%"]
```

Group A
FORWARD : _148.379_ meV _8.35698_ μm _22.4956_%
REVERSE :_132.059_ meV _9.38974_ μm _60.1608_%
****
****

Group B
FORWARD : _141.801_ meV _8.74463_ μm _62.1549_%
REVERSE :_139.17_ meV _8.90993_ μm _21.7739_%
****
Results for a SP1 detector at 80K, at _-0.15_V bias
Energy lost per collision :_0.002_eV
L_p: Mean free path between semi-elastic collisions. Given as: _60_ Angstrom
L_e: Mean free path between collisions with cold electrons. Given as: _4000_ Angstrom
****
Thresholds:
****

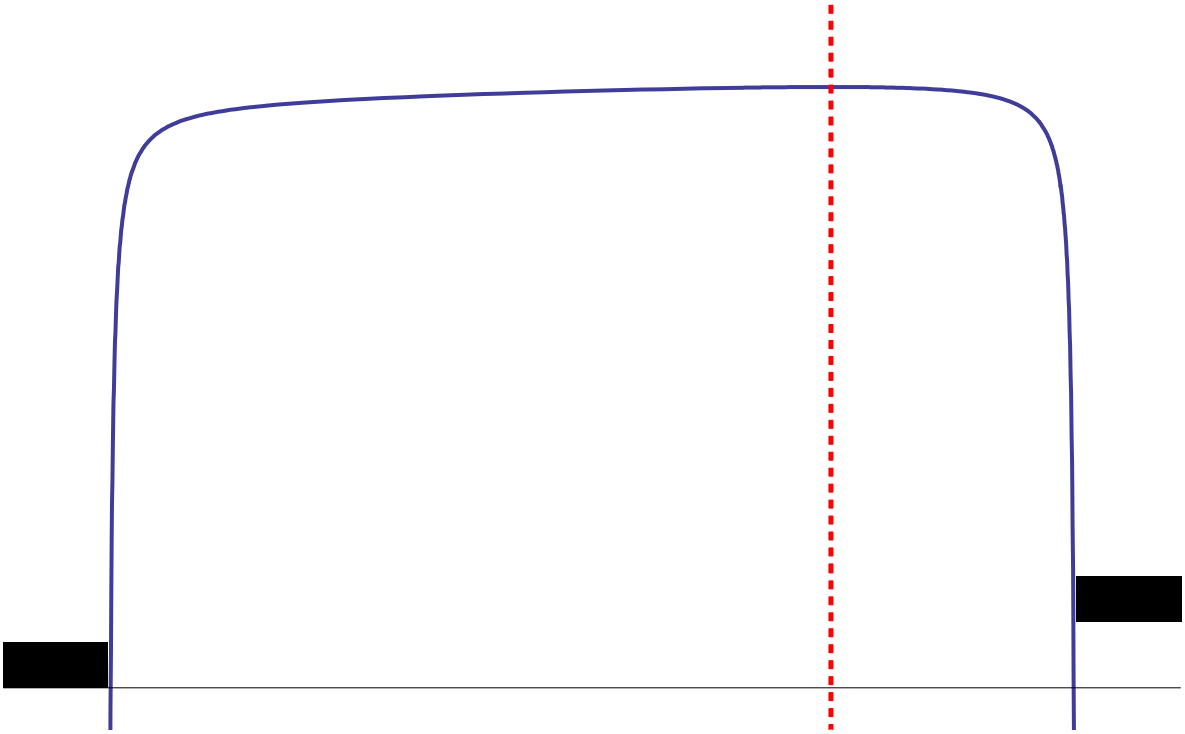

Group A
Active Layer (reverse current) :_9.38974_ μm _0.132059_ eV
Active Layer (forward current) : _8.35698_ μm _0.148379_ eV
Collector Efficiency in the Reverse direction :_60.1608_%
Collector Efficiency in the Forward direction :_22.4956_%
****

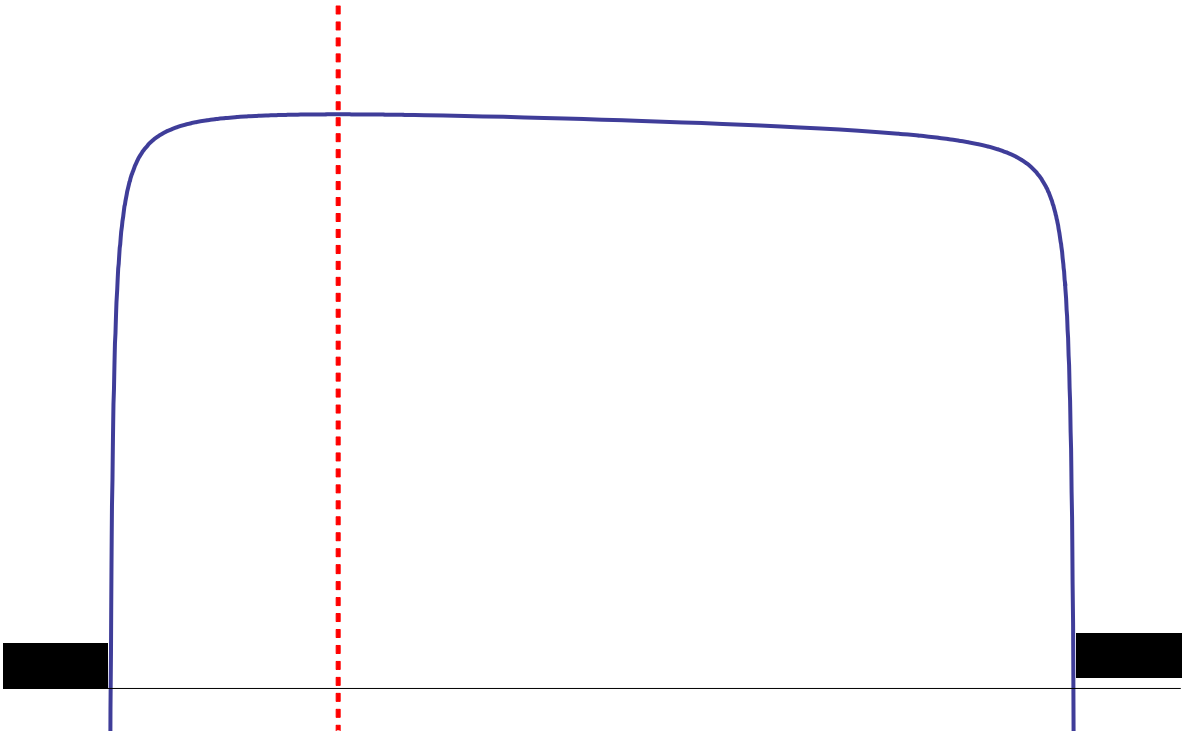

Bottom Contact (reverse current) :_8.90993_ μm _0.13917_ eV
Active Layer (reverse current) :_8.90993_ μm _0.13917_ eV
Active Layer (forward current) : _8.74463_ μm _0.141801_ eV
Collector Efficiency in the Reverse direction :_21.7739_%
Collector Efficiency in the Forward direction :_62.1549_%

ηif[photon_,vbo_,width_,ef_]:=Module[{x,y,nmax,η,ηinternal,seriesnum},
Piecewise[{
{x=0;
y=1;,
photon<vbo},
{x=(3/4)*((2/3)*((ef+photon)$^{3/2}$-(ef+vbo)$^{3/2}$)-(photon-vbo)*(ef+vbo)$^{1/2}$)/((ef+photon)$^{3/2}$-photon$^{3/2}$);
y=(1/2)*((ef+photon)$^{3/2}$-(ef+vbo)$^{3/2}$)/((ef+photon)$^{3/2}$-photon$^{3/2}$);
,photon>vbo && photon<(ef+vbo)},
{x=(3/4)*((2/3)*((ef+photon)$^{3/2}$-(photon)$^{3/2}$)-ef*(ef+vbo)$^{1/2}$)/((ef+photon)$^{3/2}$-photon$^{3/2}$);
y=(1/2);
,photon>(ef+vbo)}
}];
η[num_]:=(lstar/width)*(1-Exp[-width/lstar])$^{1/2}$*x*(photon-num*escat);
nmax=Floor[(photon-vbo)/escat];
If[nmax>100,seriesnum=100,seriesnum=nmax];
ηinternal=η[0]+Sum[(η[n]*γn)*Product[(1-(η[i]/y)),{i,0,n-1}],{n,1,50}]

]

```
emitterAbsProbGroupA=Import["c:\\output\\Final\\absorbProbEmitterGroupA.csv"];
emitterAbsProbGroupB=Import["c:\\output\\Final\\absorbProbEmitterGroupB.csv"];

bottomContactAbsProb=Import["C:\\output\\Final\\absorbProbBottomContact.csv"];



groupAreverse=emitterAbsProbGroupA;
groupAre-
verse[[All,2]]=Table[ηif[emitterAbsProbGroupA[[n,1]],groupArevwf,188,activefermi],{n,1,Len
gth[emitterAbsProbGroupA]}];
Print["Internal Photoemission Efficiency for :Group A Emitters, REVERSE current Direction"]
ListPlot[groupAreverse]
Print[" "]
groupAforward=emitterAbsProbGroupA;
groupAfor-
ward[[All,2]]=Table[ηif[emitterAbsProbGroupA[[n,1]],groupAforwf,188,activefermi],{n,1,Leng
th[emitterAbsProbGroupA]}];
Print["Internal Photoemission Efficiency for :Group A Emitters, FORWARD current Direction"]
ListPlot[groupAforward]
Print[" "]

groupBreverse=emitterAbsProbGroupB;
groupBre-
verse[[All,2]]=Table[ηif[emitterAbsProbGroupB[[n,1]],groupBrevwf,188,activefermi],{n,1,Len
gth[emitterAbsProbGroupB]}];
Print["Internal Photoemission Efficiency for :Group B Emitters, REVERSE current Direction"]
ListPlot[groupBreverse]
Print[" "]

groupBforward=emitterAbsProbGroupB;
groupBfor-
ward[[All,2]]=Table[ηif[emitterAbsProbGroupB[[n,1]],groupBforwf,188,activefermi],{n,1,Leng
th[emitterAbsProbGroupB]}];
Print["Internal Photoemission Efficiency for :Group B Emitters, FORWARD current Direction"]
ListPlot[groupBforward]
Print[" "]

bottomreverse=bottomContactAbsProb;
```

```
bottomre-
verse[[All,2]]=Table[ηif[bottomContactAbsProb[[n,1]],bottomwf,7000,contactfermi],{n,1,Lengt
h[bottomContactAbsProb]}];
Print["Internal Photoemission Efficiency for :BOTTOM CONTACT, REVERSE current Direc-
tion"]
ListPlot[bottomreverse]
Print[" "]
```

Internal Photoemission Efficiency for :Group A Emitters, REVERSE current Direction

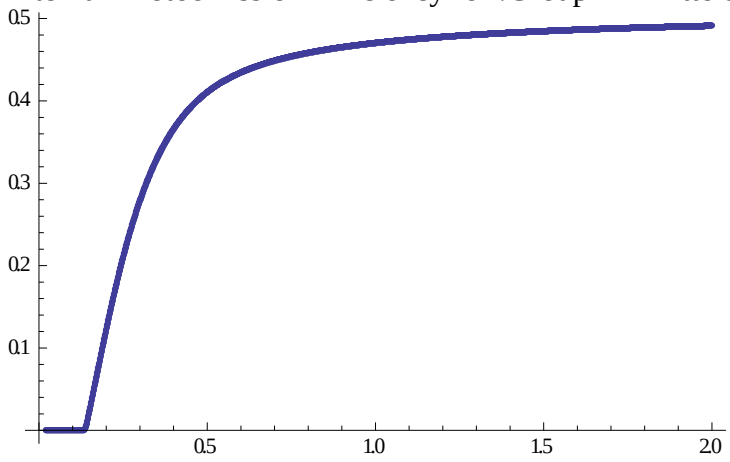

Internal Photoemission Efficiency for :Group A Emitters, FORWARD current Direction

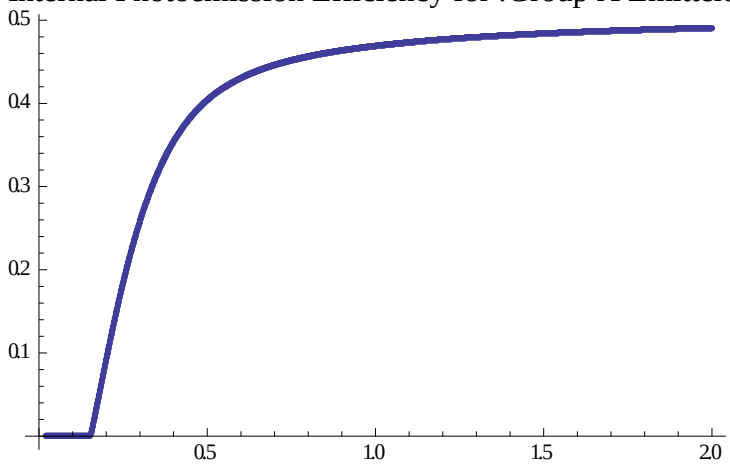

Internal Photoemission Efficiency for :Group B Emitters, REVERSE current Direction

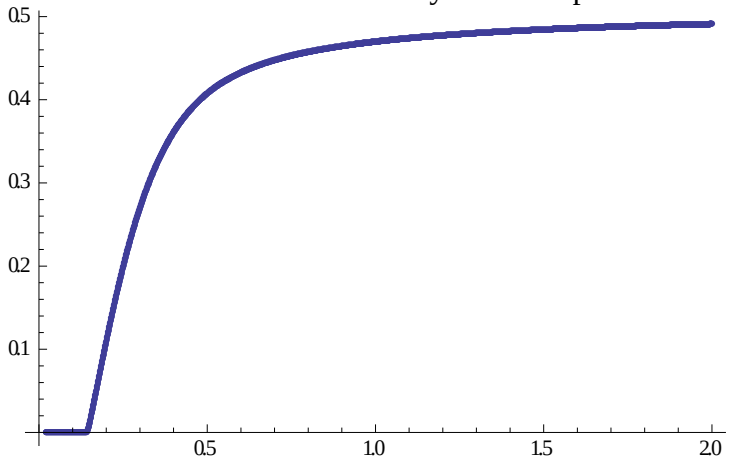

Internal Photoemission Efficiency for :Group B Emitters, FORWARD current Direction

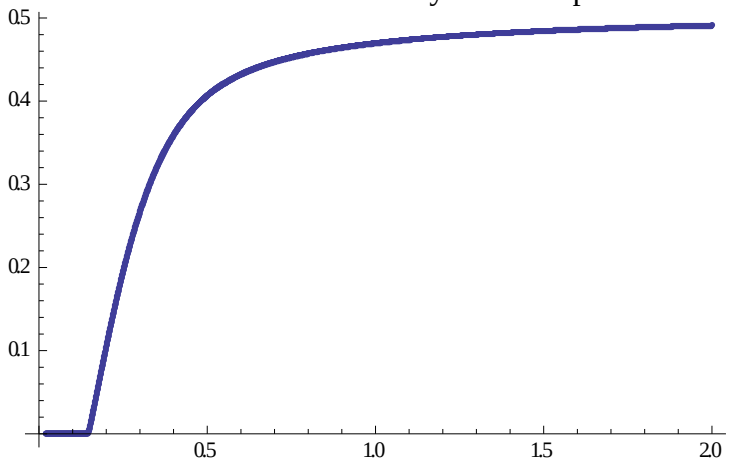

Internal Photoemission Efficiency for :BOTTOM CONTACT, REVERSE current Direction

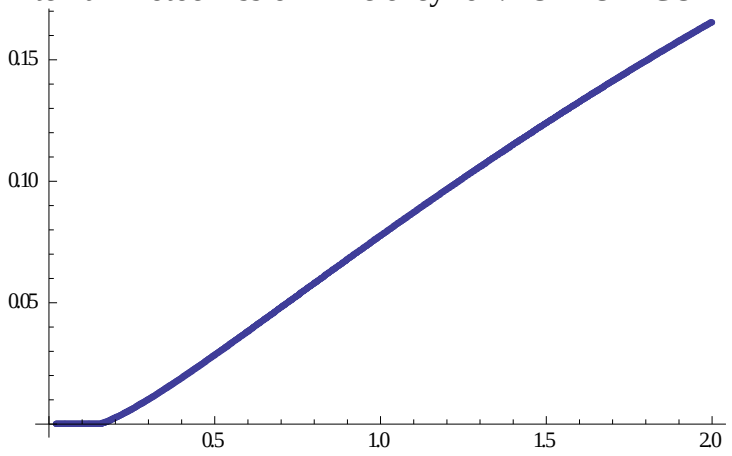

groupAforwardcurrent=groupAforward;

```
groupAforwardcur-
rent[[All,2]]=Table[(groupAforward[[n,2]]*emitterAbsProbGroupA[[n,2]]*groupAcollectorEffic
iencyForward^26)*
Sum[groupAcollectorEfficiencyForward^i,{i,1,4}],{n,1,Length[groupAforward]}];

groupAreversecurrent=groupAreverse;
groupAreversecur-
rent[[All,2]]=Table[(groupAreverse[[n,2]]*emitterAbsProbGroupA[[n,2]])*Sum[groupAcollecto
rEfficiencyReverse^i,{i,1,4}],{n,1,Length[groupAreverse]}];

groupBforwardcurrent=groupBforward;
groupBforwardcurrent[[All,2]]=Table[(groupBforward[[n,2]]*emitterAbsProbGroupB[[n,2]])*
Sum[groupBcollectorEfficiencyForward^i,{i,1,26}],{n,1,Length[groupBforward]}];

groupBreversecurrent=groupBreverse;
groupBreversecur-
rent[[All,2]]=Table[(groupBreverse[[n,2]]*emitterAbsProbGroupB[[n,2]]*groupBcollectorEffici
encyReverse^5)*Sum[groupBcollectorEfficiencyReverse^(i-
1),{i,1,26}],{n,1,Length[groupBreverse]}];


bottomcurrent=bottomreverse;
bottomcur-
rent[[All,2]]=Table[(bottomreverse[[n,2]]*bottomContactAbsProb[[n,2]])*groupBcollectorEffici
encyReverse^26*groupAcollectorEfficiencyReverse^5,{n,1,Length[bottomreverse]}];

totalforward=groupAforwardcurrent;
totalfor-
ward[[All,2]]=Table[groupAforwardcurrent[[n,2]]+groupBforwardcurrent[[n,2]],{n,1,Length[tot
alforward]}];
totalreverse=groupAreversecurrent;
totalre-
verse[[All,2]]=Table[groupAreversecurrent[[n,2]]+groupBreversecurrent[[n,2]]+bottomcurrent[[
n,2]],{n,1,Length[totalreverse]}];


totalcurrent=totalforward;
totalcurrent[[All,2]]=Table[totalforward[[n,2]]-totalreverse[[n,2]],{n,1,Length[totalcurrent]}];


groupAforwardcur-
rent[[All,1]]=Table[1.24/groupAforwardcurrent[[n,1]],{n,1,Length[groupAforwardcurrent]}];
groupAreversecur-
rent[[All,1]]=Table[1.24/groupAreversecurrent[[n,1]],{n,1,Length[groupAreversecurrent]}];
groupBforwardcur-
rent[[All,1]]=Table[1.24/groupBforwardcurrent[[n,1]],{n,1,Length[groupBforwardcurrent]}];
```

```
groupBreversecur-
rent[[All,1]]=Table[1.24/groupBreversecurrent[[n,1]],{n,1,Length[groupBreversecurrent]}];
bottomcurrent[[All,1]]=Table[1.24/bottomcurrent[[n,1]],{n,1,Length[bottomcurrent]}];

totalforward[[All,1]]=Table[1.24/totalforward[[n,1]],{n,1,Length[totalforward]}];
totalreverse[[All,1]]=Table[1.24/totalreverse[[n,1]],{n,1,Length[totalreverse]}];



totalcurrent[[All,1]]=Table[1.24/totalcurrent[[n,1]],{n,1,Length[totalcurrent]}];



Print["**********************************************************************"]
Print["Total Yields for the Individual Contributions "]
Print["RED- GROUP A Forward Current"]
Print["ORANGE- GROUP A Reverse Current"]
Print["BLUE- GROUP B Forward Current"]
Print["PURPLE- GROUP B Reverse Current"]
Print["GREEN- BOTTOM CONTACT reverse current"]
Show[ListPlot[groupAforwardcurrent,PlotStyle→
Red,PlotRange→{{1,12},{0,.0003}}],ListPlot[groupAreversecurrent,PlotStyle→ Or-
ange],ListPlot[groupBforwardcurrent,PlotStyle→
Blue],ListPlot[groupBreversecurrent,PlotStyle→ Purple],ListPlot[bottomcurrent,PlotStyle→
Green]]
Print["**********************************************************************"]
Print["Forward and Reverse Yield Comparison"]
Print["BLUE- TOTAL FORWARD CURRENT"]
Print["RED- TOTAL REVERSE CURRENT"]
Show[ListPlot[totalforward,PlotStyle→
Blue,PlotRange→{{1,12},{0,.0003}}],ListPlot[totalreverse,PlotStyle→ Red]]
Print["TOTAL YIELD:"]
ListPlot[totalcurrent,PlotRange→ {{6,7},{-.00001,.00001}}]
**********************************************************************
Total Yields for the Individual Contributions
RED- GROUP A Forward Current
ORANGE- GROUP A Reverse Current
BLUE- GROUP B Forward Current
PURPLE- GROUP B Reverse Current
GREEN- BOTTOM CONTACT reverse current
```

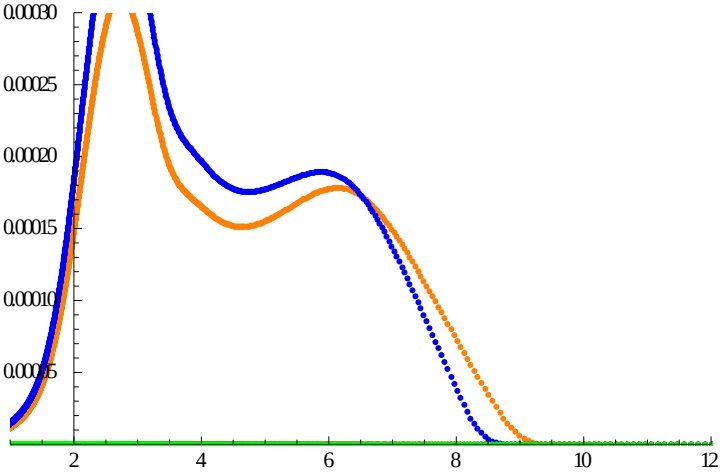

****

Forward and Reverse Yield Comparison
BLUE- TOTAL FORWARD CURRENT
RED- TOTAL REVERSE CURRENT

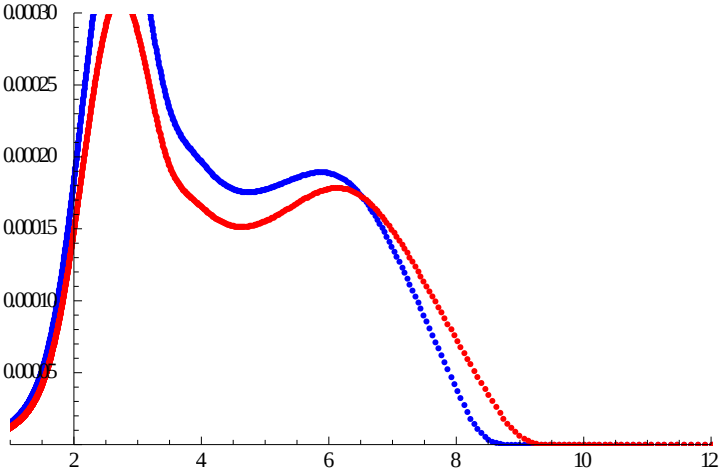

TOTAL YIELD: